PB98-107519

RELATION OF ACOUSTIC EMISSION SIGNALS TO MICROFAILURE EVENTS

AUG 97

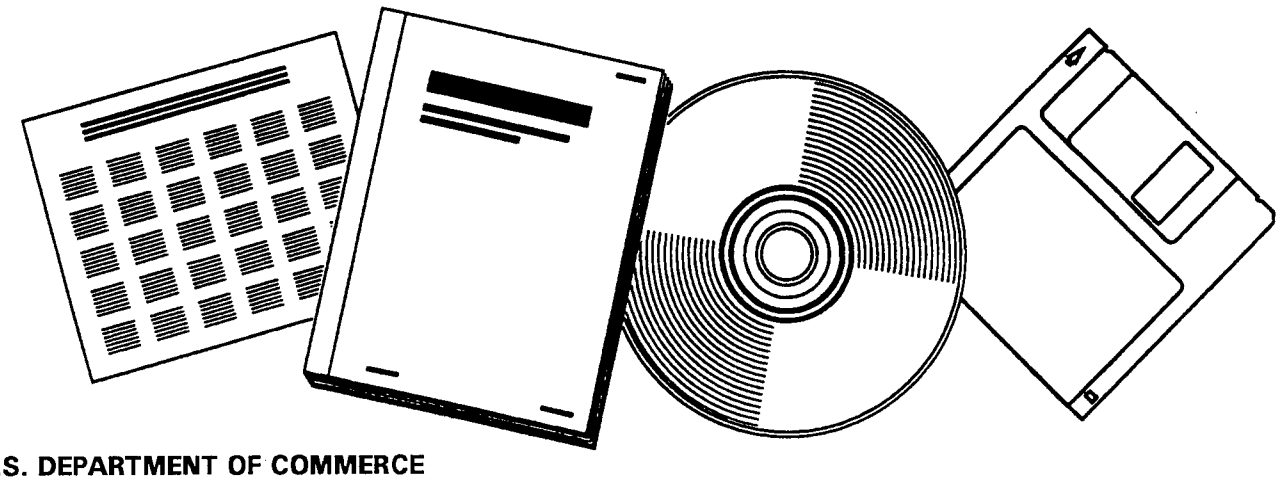

U.S. DEPARTMENT OF COMMERCE
National Technical Information Service

Relation of Acoustic Emission Signals to Microfailure Events

PUBLICATION NO. FHWA-RD-96-203

PB98-107519

AUGUST 1997

U.S. Department of Transportation
Federal Highway Administration

Research and Development
Turner-Fairbank Highway Research Center
6300 Georgetown Pike
McLean, VA 22101-2296

FOREWORD

This report, *Relation of Acoustic Emission Signals to Microfailure Events*, presents the results of research conducted for the Federal Highway Administration under a grant agreement with SRI International, Menlo Park, CA.

The research aims at enhancing the practical use of acoustic emission (AE) as an option for monitoring highway bridge integrity. AE technology is currently limited in its ability to distinguish between relevant noise (from cracking events) and extraneous noise (such as from fretting produced by bridge traffic and wind loading). It is also limited in its ability to indicate the location of AE events and the characteristics of the cracking event. By attempting to develop a better understanding of the material microfailure events that produce acoustic signals, this FHWA program seeks to reduce these limitations and thereby move AE technology toward a practical nondestructive method for continuous evaluation of the Nation's bridges. The approach was to monitor AE in a laboratory fracture test, apply a quantitative fracto-graphic technique to identify microfailure events and the sequence in which they occur, and then to correlate microfailures with the size and shape of AE signals.

This report describes the procedures and presents results from two initial studies—the first on a structural ceramic and the second on a weld in bridge steel. Although a one-to-one correlation was not achieved for the ceramic, a route for identifying microfailure origins of acoustic emission was demonstrated. For the steel weld, the early AE signals correlated with surfaces within a field of fine dimples, suggesting that acoustic signals are produced by brittle cleavage of certain grains in the steel microstructure. This effort allows important and heretofore unobtainable information about fracture evolution to be extracted from AE spectra and enhances the usefulness of AE monitoring of the Nation's bridges.

Charles J. Nemmers, P.E.
Director
Office of Engineering
Research and Development

NOTICE

Technical Report Documentation Page

1. Report No.	2. Government Accession No.	3. Recipient 's Catalog No.
FHWA-RD-96-203		

4. Title and Subtitle	5. Report Date
RELATION OF ACOUSTIC EMISSION SIGNALS TO MICRO-FAILURE EVENTS	August 1997
	6. Performing Organization Code
7. Author(s)	8. Performing Organization Report No.
D. A. Shockey and T. Kobayashi	Project 4914
9. Performing Organization Name and Address	10. Work Unit No. (TRAIS)
SRI International 333 Ravenswood Avenue Menlo Park, CA 94025-3493	11. Contract or Grant No. DTFH61-93-X-00037
12. Sponsoring Agency Name and Address	13. Type of Report and Period Covered
Office of Engineering R&D Federal Highway Administration 6300 Georgetown Pike McLean, VA 22101-2296	Final Technical Report 7/19/93 to 12/31/94
	14. Sponsoring Agency Code

15. Supplementary Notes

Contracting Officer's Technical Representative (COTR) — Mr. Richard Livingston.

16. Abstract

The Office of Advanced Research of the Federal Highway Administration is sponsoring a research program aimed at enhancing the practical use of acoustic emission (AE) as an option for monitoring highway bridge integrity. SRI International is assisting the effort by attempting to develop a better understanding of the material microfailure events that produce acoustic signals. SRI's approach was to monitor AE in a laboratory fracture test, apply a quantitative fractographic technique, FRASTA, to identify microfailure events and the sequence in which they occur, and then to correlate microfailures with AE signals. Success would provide the ability to determine important characteristics of fracturing from the size and shape of the AE signals. This report describes the procedures and presents results from two initial studies, the first on a structural ceramic and the second on a weldment in bridge steel. Although a one-to-one correlation was not achieved for the ceramic, a route for identifying microfailure origins of acoustic emission was demonstrated. For the steel weldment, the early AE signals correlated with smooth faceted transgranular surfaces within a field of fine dimples, suggesting that acoustic signals are produced by brittle cleavage of certain grains in the steel microstructure. Future work will correlate microfailure in unwelded bridge steels with AE waveforms.

17. Key Words		18. Distribution Statement
Fractography FRASTA	Acoustic emission Microfailure	No restrictions. This document is available to the public through the National Technical Information Service, Springfield, Virginia 22161.

19. Security Classi. (of this report)	20. Security Classi. (of this page)	21. No. of Pages	22. Price
Unclassified	Unclassified	53	

Form DOT F 1700.7

CONVERSION CHART

Conversion factors for U. S. Customary to metric (SI) units of measurement

MULTIPLY → TO GET	BY		← TO GET DIVIDE
angstrom	1.000 000	X E -10	meters (m)
atmosphere (normal)	1.013 25	X E +2	kilo pascal (kPa)
bar	1.000 000	X E +2	kilo pascal (kPa)
barn	1.000 000	X E -28	meter^2 (m^2)
British thermal unit (thermochemical)	1.054 350	X E +3	joule (J)
calorie (thermochemical)	4.184 000		joule (J)
cal (thermochemical)/cm^2	4.184 000	X E -2	mega joule/m^2 (MJ/m^2)
curie	3.700 000	X E +1	*giga becquerel (GBq)
degree (angle)	1.745 329	X E -2	radian (rad)
degree Fahrenheit	$T_K = (T\ °F + 459.67)/1.8$		degree kelvin (K)
electron volt	1.602 19	X E -19	joule (J)
erg	1.000 000	X E -7	joule (J)
erg/second	1.000 000	X E -7	watt (W)
foot	3.048 000	X E -1	meter (m)
foot-pound-force	1.355 818		joule (J)
gallon (U.S. liquid)	3.785 412	X E -3	meter^3 (m^3)
inch	2.540 000	X E -2	meter (m)
jerk	1.000 000	X E +9	joule (J)
joule/kilogram (J/kg) (radiation dose absorbed)	1.000 000		Gray (Gy)
kilotons	4.183		terajoules
kip (1000 lbf)	4.448 222	X E +3	newton (N)
kip/inch^2 (ksi)	6.894 757	X E +3	kilo pascal (kPa)
ktap			newton-second/m^2
	1.000 000	X E +2	(N-s/m^2)
micron	1.000 000	X E -6	meter (m)
mil	2.540 000	X E -5	meter (m)
mile (international)	1.609 344	X E +3	meter (m)
ounce	2.834 952	X E -2	kilogram (kg)
pound-force (lbs avoirdupois)	4.448 222		newton (N)
pound-force inch	1.129 848	X E -1	newton/meter (N · m)
pound-force/inch	1.751 268	X E +2	newton-meter (N/m)
pound-force/foot^2	4.788 026	X E -2	kilo pascal (kPa)
pound-force/inch^2 (psi)	6.894 757		kilo pascal (kPa)
pound-mass (lbm avoirdupois)	4.535 924	X E -1	kilogram (kg)
pound-mass-foot^2 (moment of inertia)	4.214 011	X E -2	kilogram·meter^2 (kg·m^2)
pound-mass-foot^3	1.601 846	X E +1	kilogram/meter^3 (kg/m^3)
rad (radiation dose absorbed)	1.000 000	X E -2	**Gray (Gy)
roentgen	2.579 760	X E -4	coulomb/kilogram (C/kg)
shake	1.000 000	X E -8	second (s)
slug	1.459 390	X E +1	kilogram (kg)
torr (mm Hg, 0° C)	1.333 22	X E -1	kilo pascal (kPa)

*The becquerel (Bq) is the SI unit of radioactivity; 1 Bq = 1 event/s.

**The Gray (Gy) is the SI unit of absorbed radiation.

TABLE OF CONTENTS

	Page
TECHNICAL SUMMARY	1
CHAPTER 1: MICROSTRUCTURAL ORIGINS OF FAILURE AND ACOUSTIC EMISSION IN ALUMINA	3
BACKGROUND	3
THE FRACTURE TEST	4
ANALYSIS OF THE FRACTURE SURFACES	6
CORRELATION OF MICROFAILURE EVENTS WITH ACOUSTIC EMISSION	13
CORRELATION OF MICROCRACKING WITH MICROSTRUCTURE	17
DISCUSSION AND CONCLUSIONS	24
CHAPTER 2: ACOUSTIC EMISSION SOURCES IN WELDED BRIDGE STEEL DEDUCED FROM FRACTURE SURFACE TOPOGRAPHY ANALYSIS (FRASTA)	27
BACKGROUND	27
SPECIMEN MATERIAL AND FRACTURE TEST	28
FRACTOGRAPHIC ANALYSIS	31
DISCUSSION	45
APPENDIX: THE FRASTA TECHNIQUE	47
REFERENCES	49

LIST OF FIGURES

Figure		Page
1	Acoustic events recorded as a function of increasing load during test	5
2	SEM micrograph of the fracture surface near the Vickers indentation and the crack origin	5
3	Macro-SEM photographs of conjugate fracture surfaces of an alumina four-point-bend sample. (FRASTA was applied to the framed area, which includes the Vickers indentation site; arrows indicate the crack propagation direction.)	7
4	Three-dimensional view of conjugate fracture surfaces	8
5	A series of FAPP's showing microfailure activity near the Vickers indentation. (White areas indicate separated material; black areas indicate intact material.)	10
6	Fractured area increase as a function of conjugate surface spacing	12
7	Position of the crack front at the onset of rapid crack propagation (at a topographic spacing of 0.568) as deduced from figure 6	14
8	Crack profile along the line A-A shown in figure 7	14
9	Number of microfailure nucleation events as a function of conjugate surface spacing	16
10	Superposition of FAPP's over SEM micrograph of fracture surface showing the relationship between gap formation and microstructure	18
11	Early microfailure sites and fracture surface features	20
12	Geometry and dimensions of notched round bar specimen with AE sensors and wave guides	30
13	Load versus average crack frace displacement. AE events are indicates. (The last two open circles represent four AE events)	30
14	SEM photographs of conjugate fracture surfaces	32
15	Gray-scale topography images of conjugate fracture surfaces of circumferentially fatigue-cracked tensile specimen	33

16 A series of FAPP's showing the microfracture processes in the circumferentially fatigue-precracked tensile specimen 34

17 Fractured area increase as a function of conjugate surface spacing 37

18 Superposition of FAPP's at various topographs spacings on the SEM photograph of the fracture surface 38

19 SEM micrographs of the area where FRASTA indicated first microcrack formation 41

20 SEM micrograph of the area where FRASTA detected second microcrack formation 42

21 SEM micrographs of the area where FRASTA detected third microcrack forming 43

22 SEM micrographs of fourth area where FRASTA predicted microcracking activity 44

TECHNICAL SUMMARY

The Office of Advanced Research of the Federal Highway Administration is sponsoring a research program aimed at enhancing the practical use of acoustic emission (AE) as an option for monitoring highway bridge integrity.(1) AE technology is currently limited in its ability to distinguish between relevant noise (resulting from cracking events) and extraneous noise (such as from fretting produced by bridge traffic and wind loading). It is also limited in its ability to indicate the location of AE events and the characteristics of the cracking event. This FHWA program attempts to reduce these limitations and thereby move AE technology toward a practical nondestructive method for continuous evaluation of the Nation's bridges.

The FHWA program has three goals. One goal is to develop a high-fidelity broad band (20 kHz to 1.2 MHz) AE sensor; a second goal is to produce a high digital bandwidth (1.5 Gigabit per second) signal acquisition and storage system. That work is being performed by colleagues at the National Institute for Standards and Technology and the University of Denver.(2) A third program goal is to develop a better understanding of the material microfailure events that produce acoustic signals. For this purpose, a quantitative fractographic technique, fracture surface topography analysis (FRASTA), was applied to identify microfailure events and correlate them with AE signals. Success would provide the ability to determine important characteristics of fracturing from the size and shape of the AE signals. A current summary of progress is provided in reference 1.

This report describes the FRASTA effort and presents results from two initial studies, the first on a structural ceramic and the second on a weldment in bridge steel. Other work is being performed on bridge steel grades A36, A572, and A7.

The first phase of this project was to show the feasibility of the FRASTA technique for evaluating AE spectra by applying FRASTA to broken specimens of Al_2O_3 for which the acoustic activity had already been recorded. The FRASTA technique was used to quantify the topographies of the conjugate fracture surfaces and to examine the misregistries when the topographs were in their relative positions during specimen fracture. The appearance and expansion of individual misregistries as the topograph displacement was increased revealed the sequence of microfailure nucleation and growth. These results were correlated with the acoustic data in attempting to ascribe individual AE signals to specific microfailures. Although a one-to-one correlation was not achieved in this initial work, a route for identifying microfailure origins of acoustic emission was

demonstrated. The work further pinpointed the weak features in the alumina microstructure and showed how materials development efforts could be facilitated by application of FRASTA.

The second phase of this project was a similar effort to determine microstructural origins of AE in a weldment of bridge steel. A circumferentially notched and fatigue-precracked round bar tensile specimen was monotonically loaded to failure. Ten AE signals emanated from the fracture plane, which was located in the weld material. FRASTA was used to reconstruct the fracture in microscopic detail and pinpoint the sites of microfailure. The early AE signals correlated with microfailures near the fatigue precrack front. Examination of the microfailure initiation sites at high resolution revealed smooth faceted transgranular surfaces within a field of fine dimples, suggesting that acoustic signals are produced by brittle cleavage of certain grains in the steel microstructure.

CHAPTER 1: MICROSTRUCTURAL ORIGINS OF FAILURE AND ACOUSTIC EMISSION IN ALUMINA

The nucleation sites, growth paths, and order of sequence of the microfailures that produced the macrocrack in a four-point-bend specimen of alumina were investigated by analyzing misregistries in the topographies of the conjugate macrocrack surfaces. An attempt was made to correlate these results with microstructural features and with acoustic signals recorded during the fracture test. The fracture surface topography analysis technique showed how internal interfaces control fracture and how individual acoustic emission signals might be relatable to specific microfailure events.

BACKGROUND

Despite renewed interest and a vigorous worldwide research and development effort over the past 10 years to enhance the toughness of ceramic materials, the inherent poor resistance of ceramics to fracture has been improved only marginally and the use of ceramics in fracture-susceptible applications has not increased substantially. Toughening schemes based on refined grain size, elongated grain structures, crack tip phase transformations, incorporation of strong fibers or ductile phases, and the like have produced limited success, but do not allow for the use of ceramics in many applications where, because of their superior high temperature strength, oxidation and corrosion resistance, or low density, ceramics would be chosen over metallic or polymeric materials.

Fundamental to success in toughening ceramics are (1) an understanding of how microcracks form, grow, and coalesce in a ceramic microstructure and (2) a way to monitor the effects of compositional or microstructural modifications on the microcracking processes as they occur in the interior of the ceramic. This project applied a fracture surface analysis technique to attempt to reconstruct the microfailure activity that occurred in a four-point-bend specimen of alumina. The microfailure nucleation sites, growth paths, and coalescence events indicated by the analysis were correlated with microstructural features to establish weak and tough locations in the ceramic and thereby provide insight to the material synthesizer regarding measures for toughening the microstructure. Furthermore, the type, extent, and order of occurrence of microfailure events obtained from the analysis was used in an attempt to correlate the acoustic signals recorded during

the test. If individual acoustic signals can be traced to the microfailure event that caused them, the usefulness of acoustic emission (AE) monitoring for interpreting microfracture in a specimen interior will be enhanced.

THE FRACTURE TEST

The fracture tests conducted at the University of Denver by M. Hamstad et al. are described in references 3 and 4. A synopsis is presented here. Four-point-bend specimens, 12 cm long and 10.16 by 7.62 mm^2 in cross section, were precision ground from fine-grained (2 μm) alumina plate material supplied by Alcoa laboratories. Details of the processing and microstructure were not provided. However, the fracture surfaces (see figures 2 and 11) show large, equiaxed agglomerates and pores between the agglomerates, suggesting that the material was consolidated (probably by die pressing) from spray-dried particles. Because of incomplete agglomerate deformation and hence poor consolidation, the resultant sintered body has only about half of the strength expected from a quality ceramic of this grain size and density.

PAC Model μ 30 AE sensors were coupled to the two ends of each specimen, using vacuum grease as a couplant. A Dunegan Corporation Model 8000 microprocessor-based AE system was used to measure arrival times and propagation velocities.

The specimens were carefully aligned in a test fixture and then loaded in an Instron machine at a constant crosshead rate of 0.05 mm/min. Preliminary attempts to record acoustic signals were complicated by extraneous noise from the machine, load train, and grips. After proof cycling to a load of 1780 N several times to eliminate AE at low loads, a smooth, four-sided pit was introduced in the midregion of the specimen by indenting with a Vickers diamond pyramid indentor at a load of 98 N. According to indentation theory and numerous experimental observations, a 98 N Vickers indent in alumina generates about 175-micron deep radial crack centered about the indent. For this poorly consolidated material, however, no cracking was observed around the indent.

The indented specimen was then loaded monotonically in four-point bending with the indentation on the tensile surface; AE signals were recorded until fracture occurred at a load of 1580 N. Figure 1 shows the AE results (31 events were recorded). The peak amplitudes are small. Additional events may have been recorded with a more sensitive AE system. Peak amplitudes did not increase as the damage grew, suggesting larger growth steps do not occur as the load increases. The data are thus consistent with a macrocrack growth mechanism that assumes

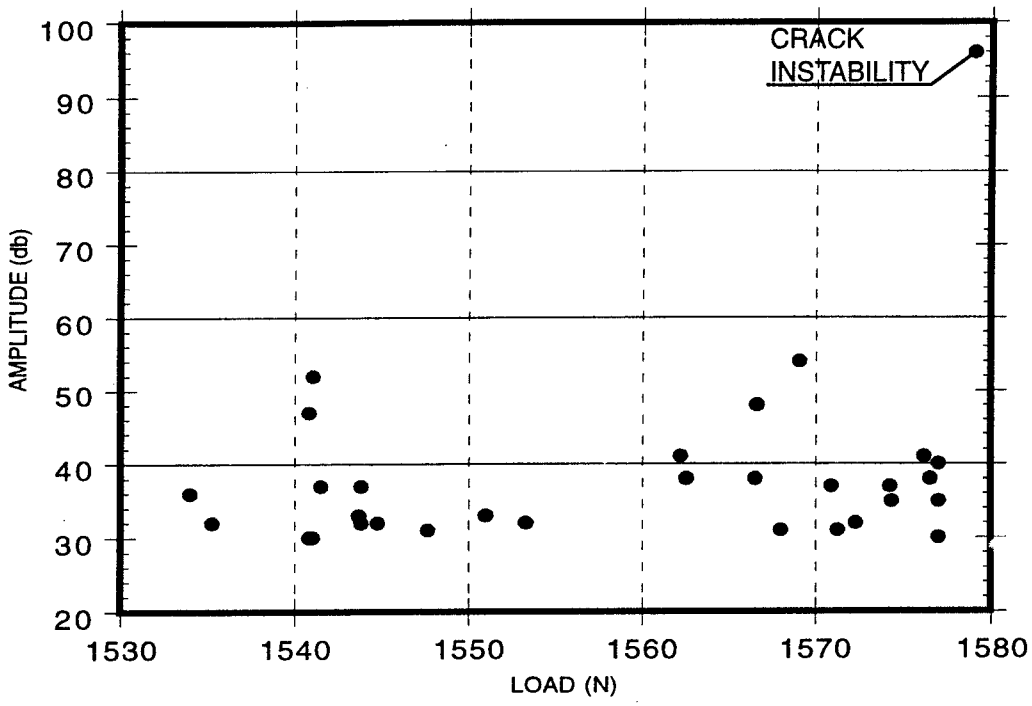

Figure 1. Acoustic events recorded as a function of increasing load during test.

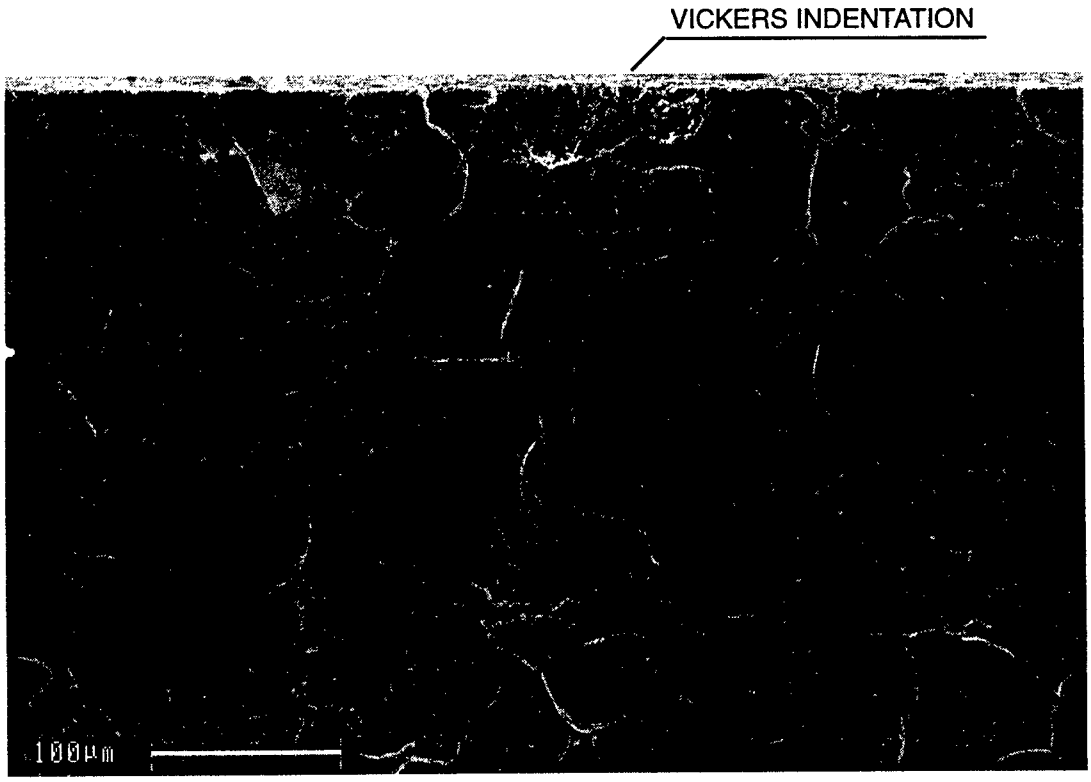

Figure 2. SEM micrograph of the fracture surface near the Vickers indentation and the crack origin.

nucleation, growth, and coalescence of similar-size microcracks immediately ahead of the macrocrack tip.

ANALYSIS OF THE FRACTURE SURFACES

Scanning electron microscope (SEM) photographs of the fracture surfaces in the vicinity of the Vickers indentation, figure 2, revealed agglomerates and agglomerate boundaries as dominant microstructural features. Low magnification photographs revealed the growth direction of the macrocrack, figure 3. The rectangular frame in figure 3 indicates the area presented in figure 2, and the arrows indicate the direction of the radial extension of the crack from the indentation. These arrows appear to emanate from a small area slightly to the left of the indentation; hence, we consider this area to be the crack origin. Fracture surface topography analysis (FRASTA) was applied to this area to delineate microfailure events and to attempt to correlate them with AE signals and microstructural features.

FRASTA entailed quantifying the topographies of the fracture surface within the two rectangles in figure 3 (labeled Surface A and Surface B), inverting one topograph and aligning it with respect to the other so that the two topographs were in the same relative position as the fracture surfaces when the surfaces separated during the fracture test, and then examining the matches and mismatches between the topographs at various relative displacements. The FRASTA technique is described in more detail in the appendix and in references 5 and 6.

A confocal-optics-based scanning laser microscope was used to characterize the topography of each fracture surface. Figure 4 shows perspective views of the conjugate fracture surfaces. These three-dimensional perspective plots show clearly the profile of the Vickers indentation on and beneath the exterior surface. The large hills on one surface fit to the valleys of the other surface, indicating that topographies of conjugate surfaces match well macroscopically. However, microscopically, gaps between the topographic surfaces exist in some areas and overlapping occurs in other areas.

Such local mismatches result from inelastic deformations as material separates. These areas are identified and differentiated in FAPP's (fractured area projection plots), which are obtained by positioning the conjugate topographs in the position of the fracture surfaces during fracture. As the displacement between the two topographs is increased, the gapped areas increase in number, grow

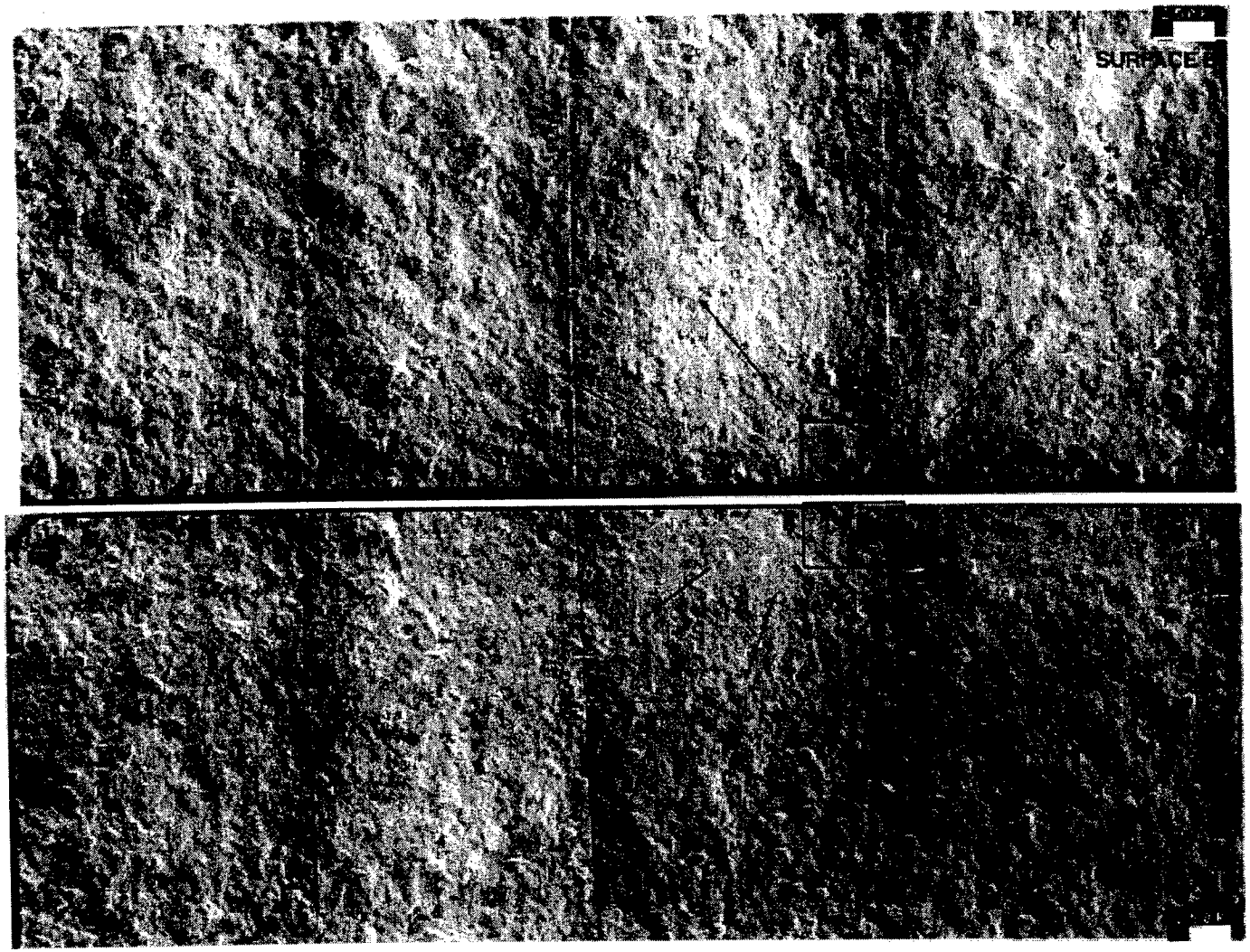

Figure 3. Macro-SEM photographs of conjugate fracture surfaces of an alumina four-point-bend sample. (FRASTA was applied to the framed area, which includes the Vickers indentation site; arrows indicate the crack propagation direction.)

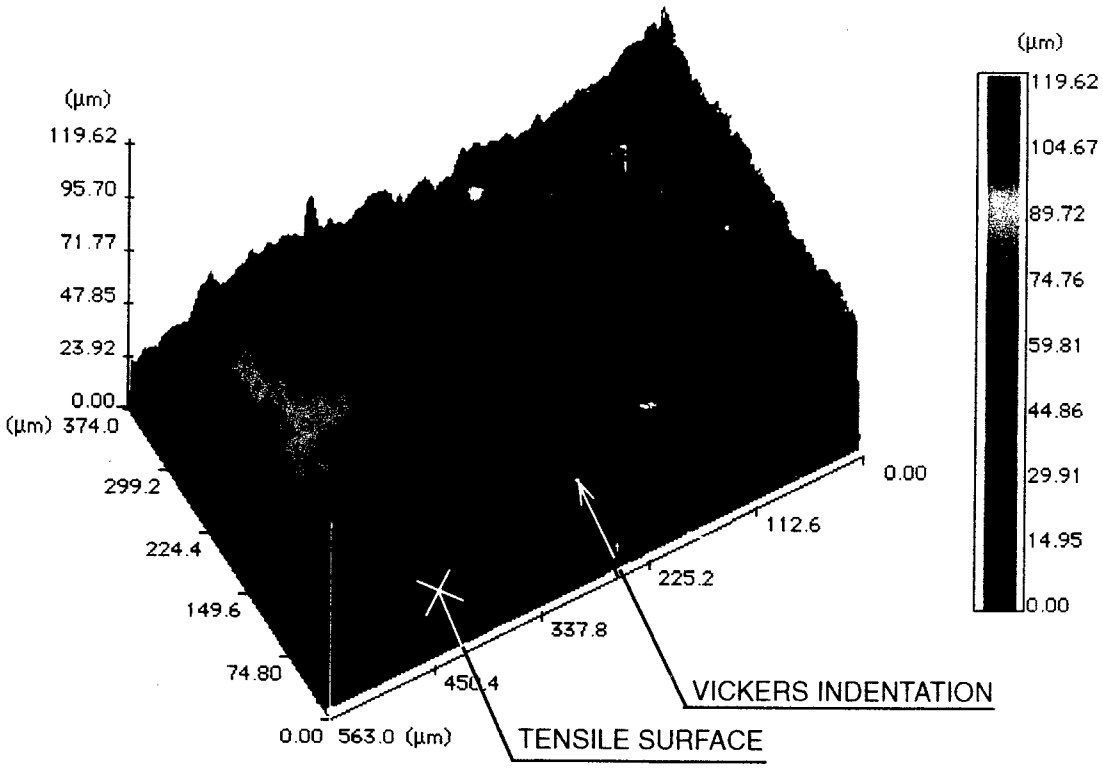

(a) Surface A

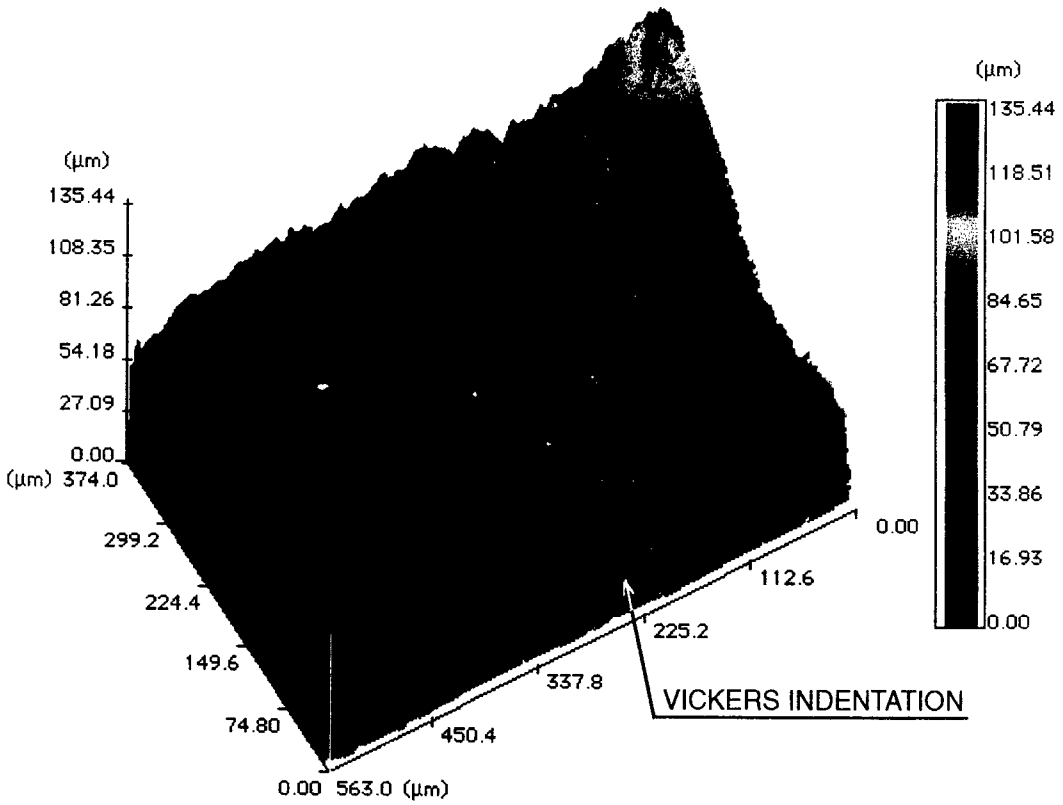

(b) Surface B

Figure 4. Three-dimensional view of conjugate fracture surfaces.

larger, and coalesce with one another. The gap evolution corresponds to microfailure development. Thus, the FAPP's are like x-radiographs of the specimen looking normal to the nominal crack plane.

Figure 5 shows a series of FAPP's. The white areas are areas where gaps between conjugate surfaces exist and, hence, represent separated material; the black areas are areas of topograph overlap and represent unbroken material. The early plots (spacing up to 0.500) show the shape of the Vickers indentation. A few isolated white areas are observed in these figures; these could be natural voids in the material. In the plot for a spacing of 0.510, some signs of microfailure are evident along the exterior (tensile) specimen surface slightly left of the indentation. In the next few plots, the early microfailure along the exterior surface starts to grow, and a few more isolated microfailures form ahead of the growing crack. Slight microfailure growth from the indentation is also indicated.

Rapid formation of microfailures and rapid growth of existing microfailures begin at a spacing of about 0.540. In the FAPP at 0.550, a crack adjacent to the indentation has grown to where it is about to coalesce with the indentation. At a spacing of 0.560, a semielliptical macrocrack is indicated. The macrocrack advances with increasing topograph separation (compare the FAPP at the spacing of 0.570). The diffuse boundary between white and black areas in the FAPP's of figure 5 shows that the crack front in alumina is not abrupt and that the fracture process zone is wide. Thus, the FAPP's indicate the locations of microcrack formation and show the instantaneous state of the fracture process.

Information on failure rate was obtained by plotting the fractured area in each FAPP as a functior. of conjugate surface spacing, figure 6. The slope of the curve indicates how fast the area is increasing. Below the spacing of 0.520, the area increase rate is low and linear. This region may represent the unloaded state of the material. However, at a spacing of about 0.520, the fractured area starts to increase, gradually at first and then more rapidly. At a spacing of about 0.568, the fractured area increase rate reaches a maximum and beyond this spacing remains constant. This maximum point is interpreted as the point of crack instability.

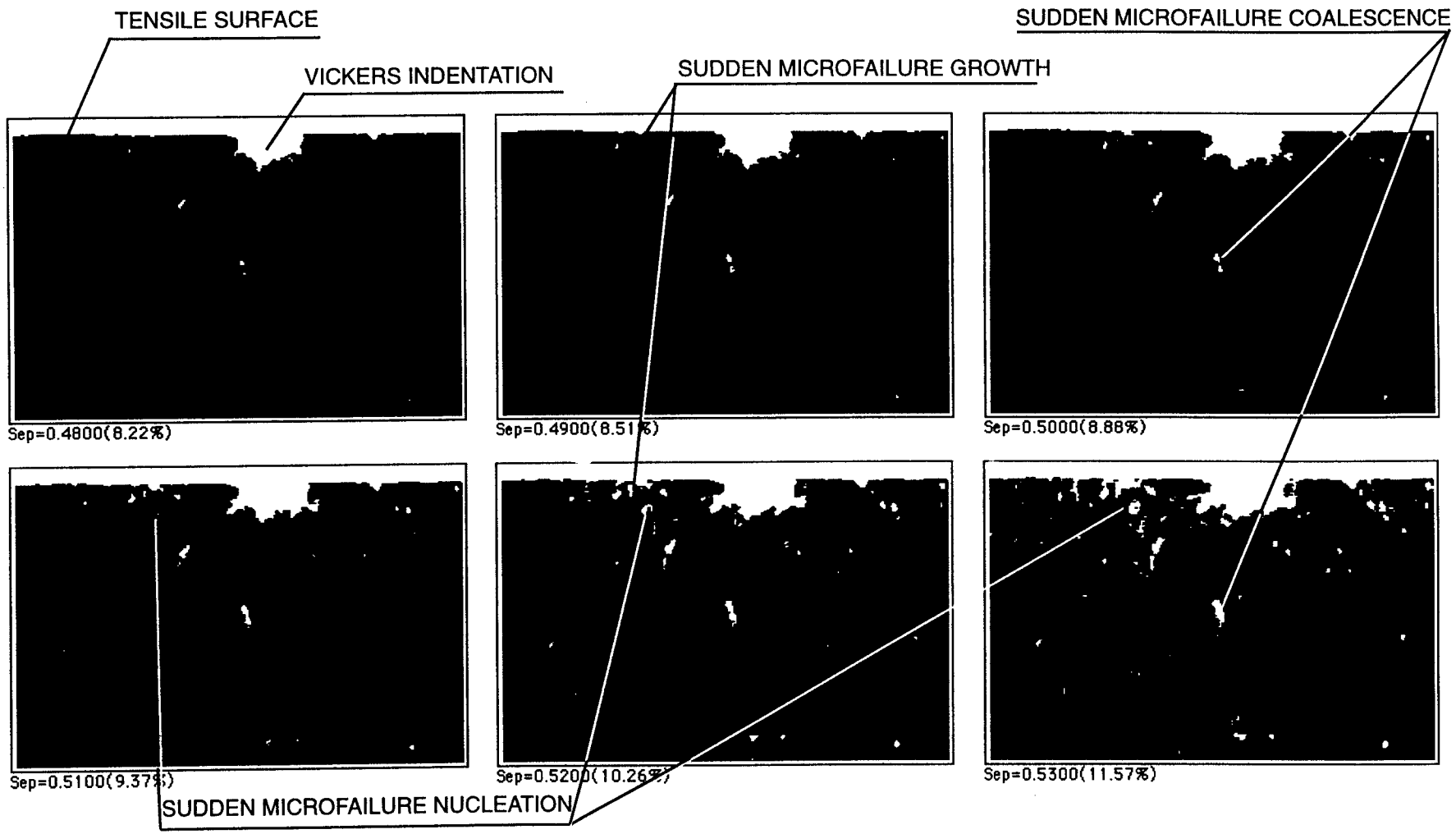

Figure 5. A series of FAPP's showing microfailure activity near the Vickers indentation. (White areas indicate separated material; black areas indicate intact material.)

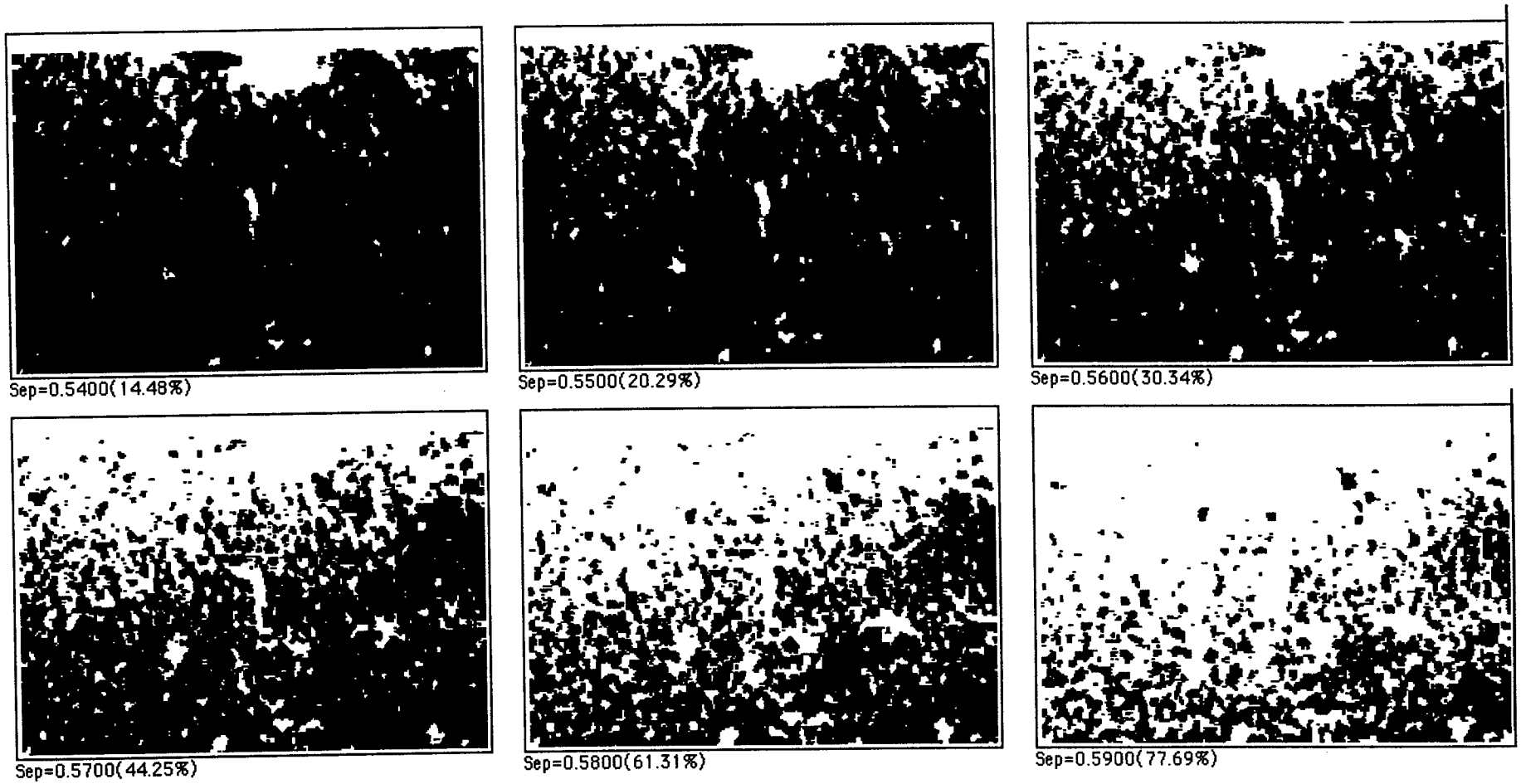

Figure 5. A series of FAPP's showing microfailure activity near the Vickers indentation (concluded). (White areas indicate separated material; black areas indicate intact material.)

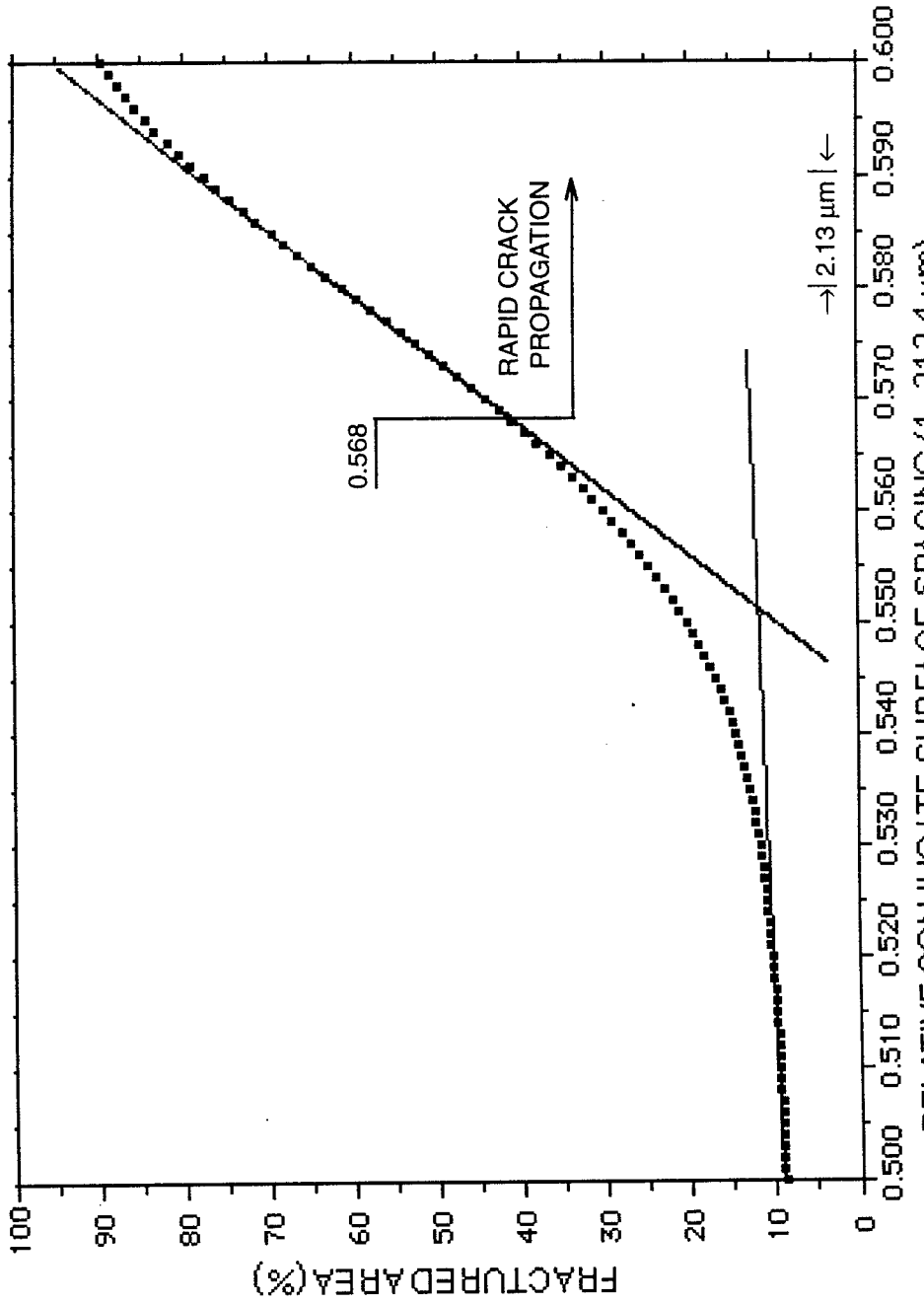

Figure 6. Fractured area increase as a function of relative conjugate topograph spacing.

Figure 7 shows the FAPP corresponding to the spacing of 0.568 (i.e., the state of fracture at the time of unstable crack propagation). Although no well-defined crack front is evident, a line separating predominantly black areas from predominantly white areas can be drawn to indicate the effective crack front position at instability. Figure 8 shows the cross-sectional plot along the line A-A. These two figures suggest that the depth of the crack at instability was about 200 μm.

The depth of the crack can be related to the stress intensity of the material and the applied load. The specimen ruptured at a maximum load of 1579 N, according to the test record provided by Professor Hamstad. Considering the four-point-bend loading condition and the specimen geometry, the maximum stress at the tensile side of the specimen was calculated to be 161 MPa. The fracture toughness of the specimen can be computed by using a simple relationship relating the stress intensity to the applied stress and the crack depth (7) shown in equation (1).

$$K_{Ic} = 0.8\sigma_c\sqrt{\pi a_c} \qquad (1)$$

where σ_c is the critical level of applied stress, a_c is the crack depth at instability, and K_{Ic} is the fracture toughness. Substituting the above values gives a fracture toughness of 3.2 MPa$\sqrt{m}$, which is somewhat less than fracture toughness values for high quality alumina found in the literature[8] and hence is a reasonable value for poorly bonded alumina such as the present material.

CORRELATION OF MICROFAILURE EVENTS WITH ACOUSTIC EMISSION

Acoustic emission signals are stress pulses that result from the sudden creation of surface within the material. Possible sources of AE in the alumina specimen examined here are microfailure nucleation (i.e., the sudden appearance of a crack), microcrack growth (i.e., the sudden enlargement of a crack), and microcrack coalescence (i.e., the sudden rupture of the ligament between two neighboring cracks). The FRASTA results in figure 5 reveal these microcracking events; an example of each possible source is indicated.

For the alumina four-point-bend specimen, the number of microfailure events indicated by FRASTA is more than an order of magnitude larger than the number of recorded AE events. Presumably the signals from most of the microcracking were too low in intensity to be detected by the transducers. If the free surface is created slowly, the stress release occurs slowly and cannot be detected by the transducer.

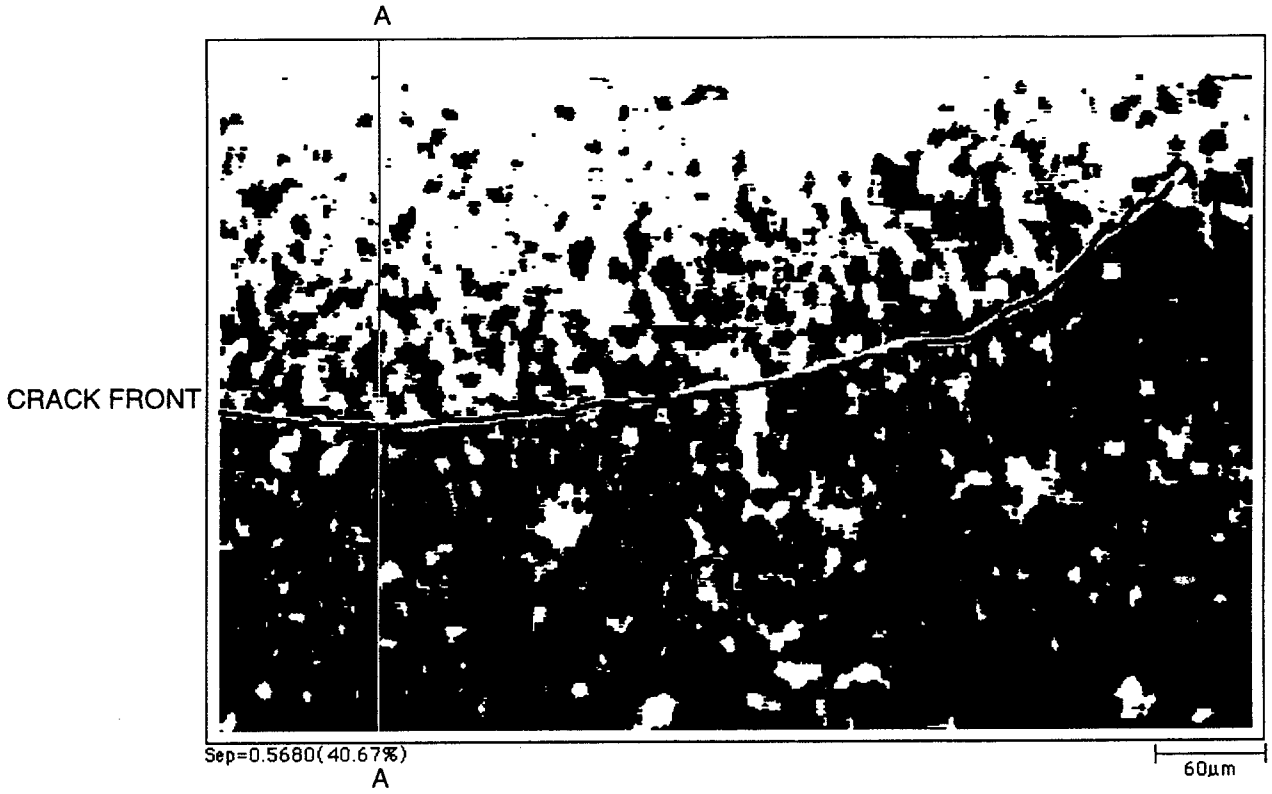

Figure 7. Position of the crack front at the onset of rapid crack propagation (at a topographic spacing of 0.568) as deduced from figure 6.

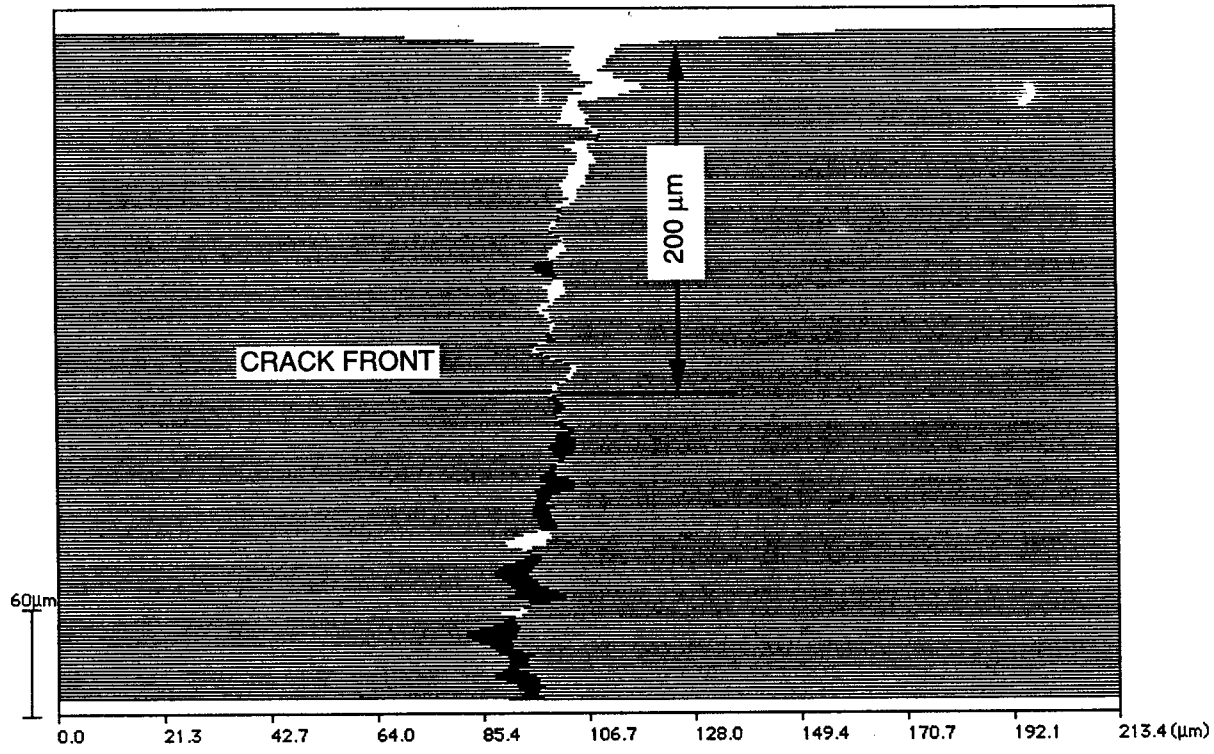

Figure 8. Crack profile along the line A-A shown in figure 7.

Attempts were made to identify the 31 microfailure events that produced detectable AE signals (figure 1) by considering the nucleation events that occurred before macrocrack instability (i.e., before a topograph spacing of 0.568). These events are shown in figure 9 as a function of topograph spacing. Because the number (281) is much larger than the number of AE signals (31), the intensity of nucleation emission from most of the microfailures was less than the intensity threshold setting of the acoustic listening system. A way is needed to identify those microfailure nucleation events that emitted strong acoustic signals. One might assume that failures in the most strongly cemented grain boundaries should produce the strongest stress waves, but although the microfailure sites could be related to microstructure features (as discussed in the next section), it was difficult to establish which microfailures produced the largest stress waves.

Those events that created the largest area were examined next on the assumption that the largest area increases might produce the largest AE signals. The largest failures in the FAPP's were identified—particularly those whose area increased most from one FAPP to another. However, most microfailures increased in area at a similar rate and, as with nucleation events, the number of such crack growth events greatly exceeded the number of AE signals. Coalescence events were also identified, particularly those that resulted in a large jump in separated area, but again no correlation could be made with the AE record.

An attempt was made to compare the number of microfailures appearing versus increasing topograph displacement shown in figure 9, with the AE signal versus load record shown in figure 1. The abscissas of the two figures were reconciled by assuming that the last data point on each plot represented the onset of macrocrack instability and hence was obtained at the same time. Then, assuming that the applied load and the crack opening (topograph) displacement increased linearly during the test, the pattern of microfailures could be compared with the pattern of AE signals. This correlation is indicated in the cracking progression plot of figure 6.

The AE data appear to occur in two groups separated by a silent period. The latter AE activity occurs as the macrocrack is reaching critical size for unstable propagation. The initial AE activity coincides with early microfailure activity near the indentation site before the macrocrack is formed. A silent period occurs between the initiation and instability phases. No acoustic signals were recorded in the very early part of the test, although FRASTA indicated that microfailure occurred then.

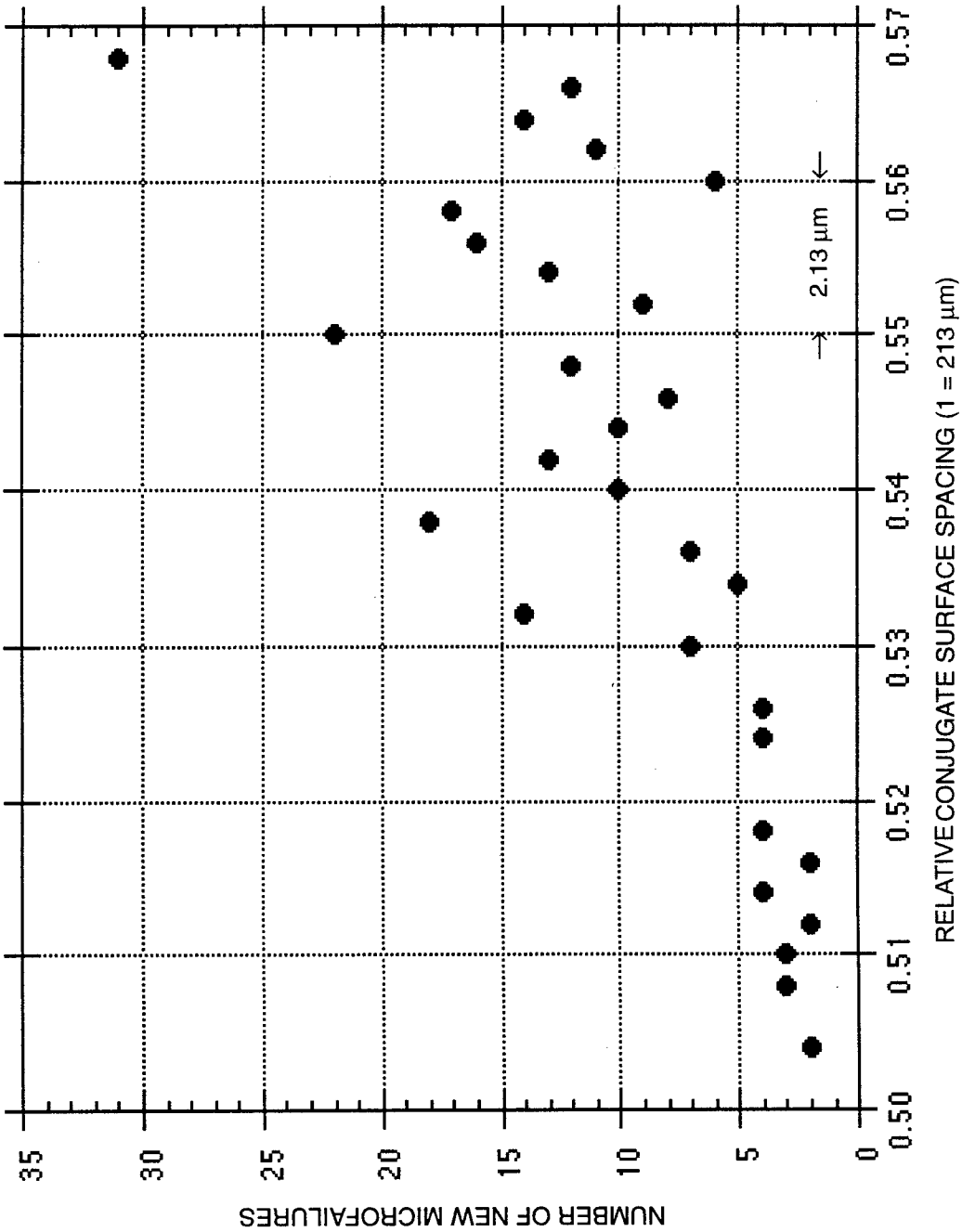

Figure 9. Number of microfailure nucleation events as a function of relative conjugate topograph spacing.

Careful visual inspection of the FAPP's reveals three regions of rapidly developing fracture surface. Each is located near the tensile edge of the specimen and each consists of a number of microfailure events. Many of the AE signals presumably emanate from these regions, but despite a more detailed examination of these areas with FRASTA, figures 10 and 11, the signals could not be related to the individual microfailures.

Thus, only general correlation trends were found between the recorded acoustic signals and the microfailure activity indicated by FRASTA. Nevertheless, this technology should make possible a one-to-one correlation between acoustic signals and the causative microfracture event. Automated image analysis equipment should be useful in quantifying and reducing the appearance, expansion, and joining rates of the gapped areas revealed in the FAPP's. Wideband acoustic sensors and advanced recording systems will allow waveforms to be recorded, which will provide information on the nature of the stress relief wave and hence the rate, orientation, three-dimensional location, and other characteristics of the microfailure event. Similar studies in metallic alloys and polymers can be expected to shed additional light on the interpretation of AE signals.

CORRELATION OF MICROCRACKING WITH MICROSTRUCTURE

The microfailure events predicted by FRASTA were correlated with the microstructure by superimposing selected FAPP's over the SEM photograph shown in figure 2. The results are shown in figure 10. Isolated white areas observed in the early stage FAPP's shown in figure 5 often correspond to voids between agglomerates (figure 10a). In other cases, the agglomerate boundaries were apparently not well fused and either existed as flaws and unbonded interfaces or were separated very early under low load with little resistance.

Figure 10b shows the state where a debond of significant size formed in the area slightly left of the indentation and along the exterior surface; figure 10c shows how the debond grew. Additional debond formation can be seen in this figure. Succeeding figures show the debonding patterns at later stages of loading.

A few areas on these plots, where early debonds were formed and where growth was faster, were examined at higher magnifications to more clearly show the relationship between debonding and microstructure. Figure 11a shows an area that exhibited early debond formation, and figure 11b is the enlargement. Clearly, early gap formation occurs preferentially at agglomerate boundaries, particularly at triple points. Figures 11c and 11d show the debond pattern after a separation of 0.548. The solid lines in the figure indicate the debond fronts observed at an

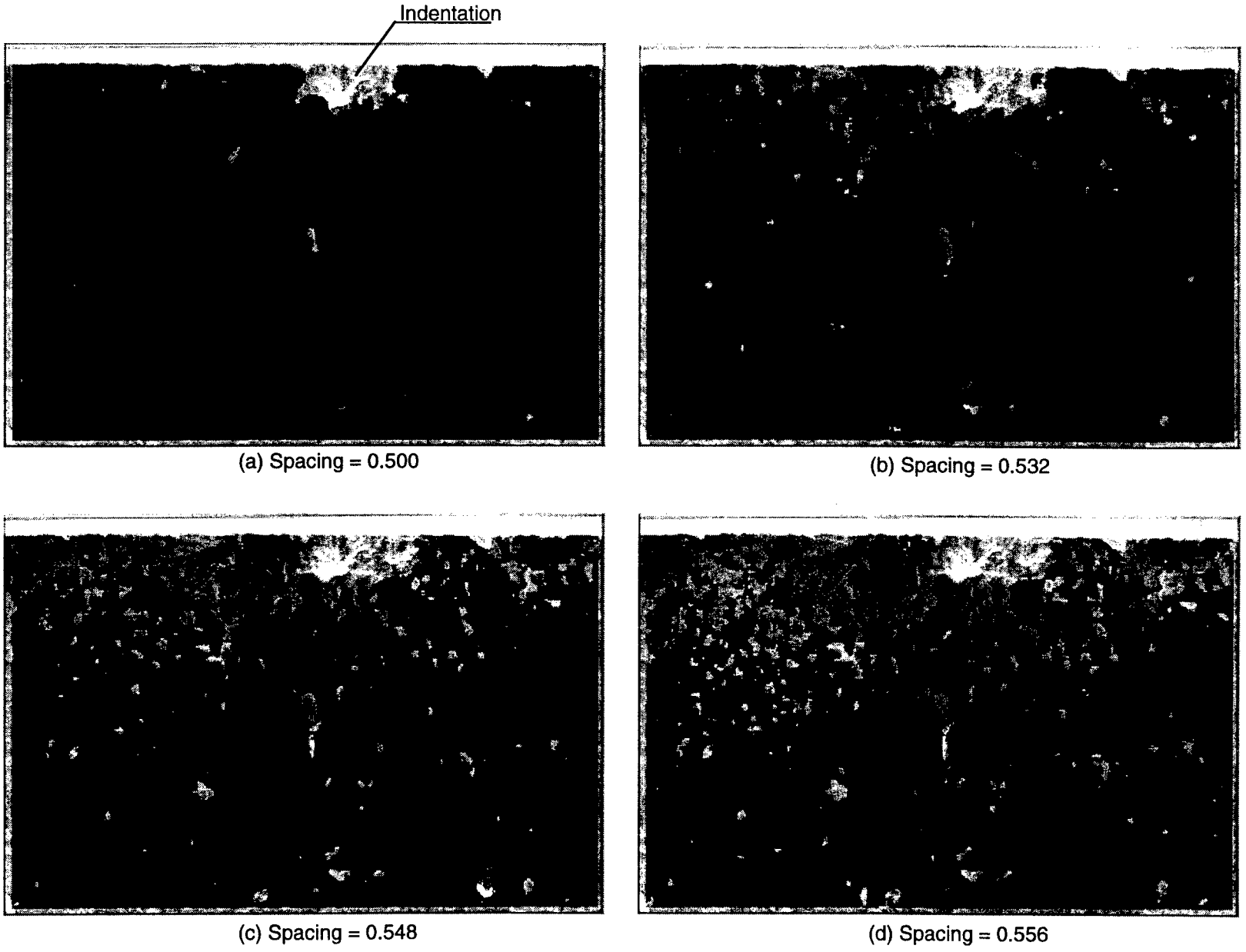

Figure 10. Superposition of FAPP's over SEM micrograph of fracture surface showing the relationship between gap formation and microstructure.

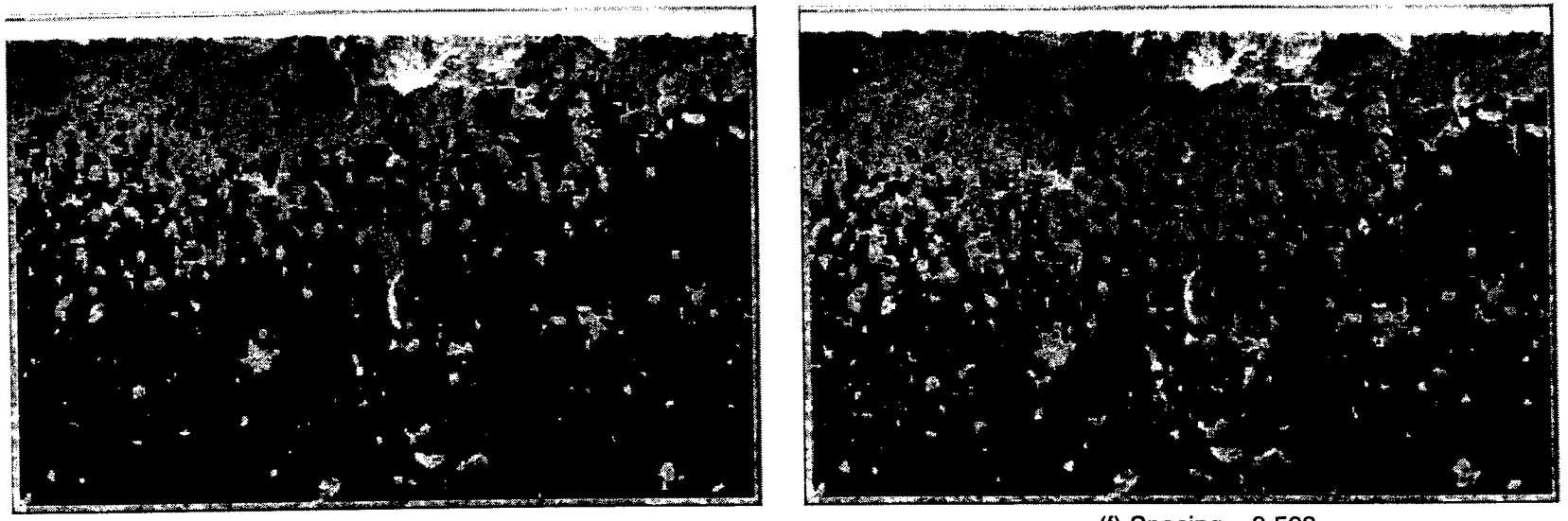

(e) Spacing = 0.562

(f) Spacing = 0.568

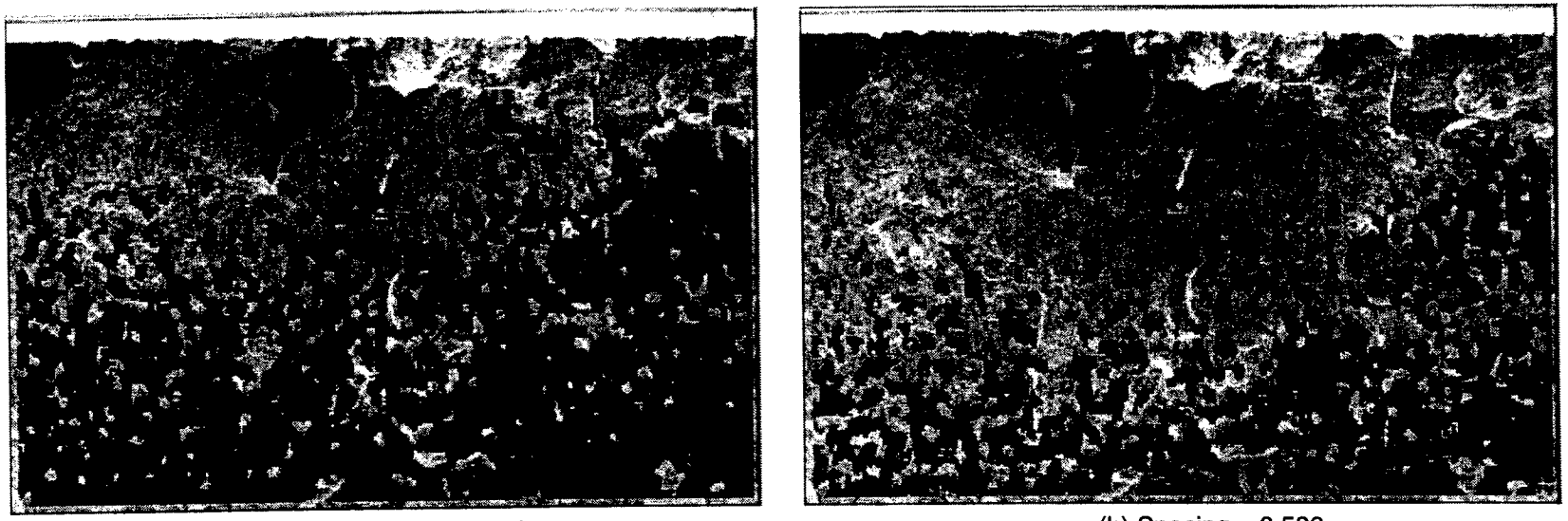

(g) Spacing = 0.574

(h) Spacing = 0.586

Figure 10. Superposition of FAPP's over SEM micrograph of fracture surface showing the relationship between gap formation and microstructure (concluded).

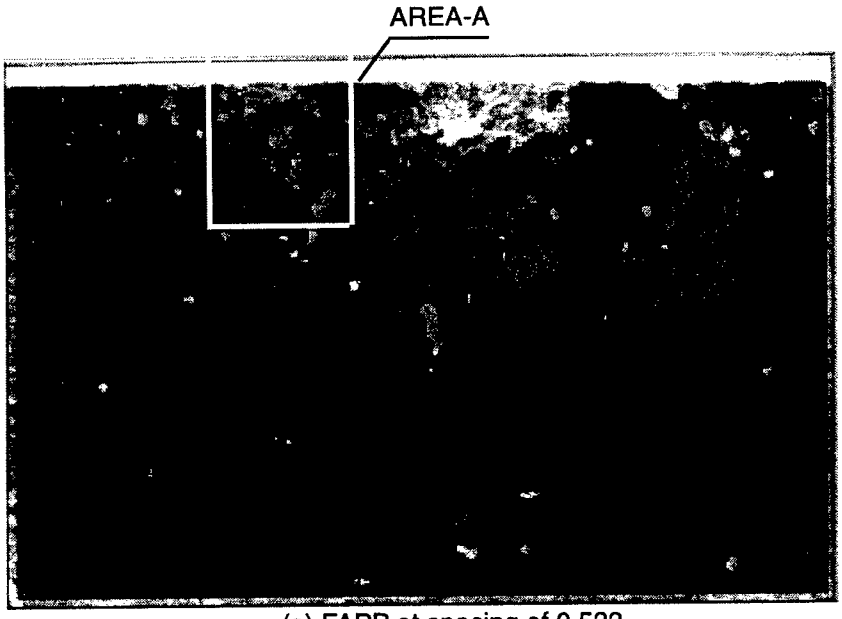

(a) FAPP at spacing of 0.532

(b) Enlargement of Area-A

Figure 11. Early microfailure sites and fracture surface features.

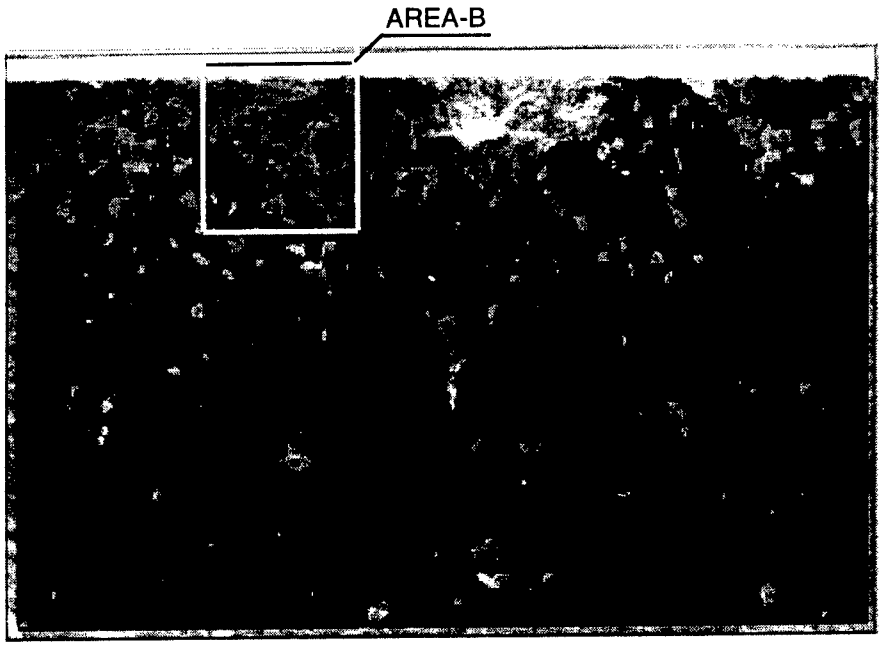

(c) FAPP at spacing of 0.548

(d) Enlargement of Area-B

Figure 11. Early microfailure sites and fracture surface features (continued).

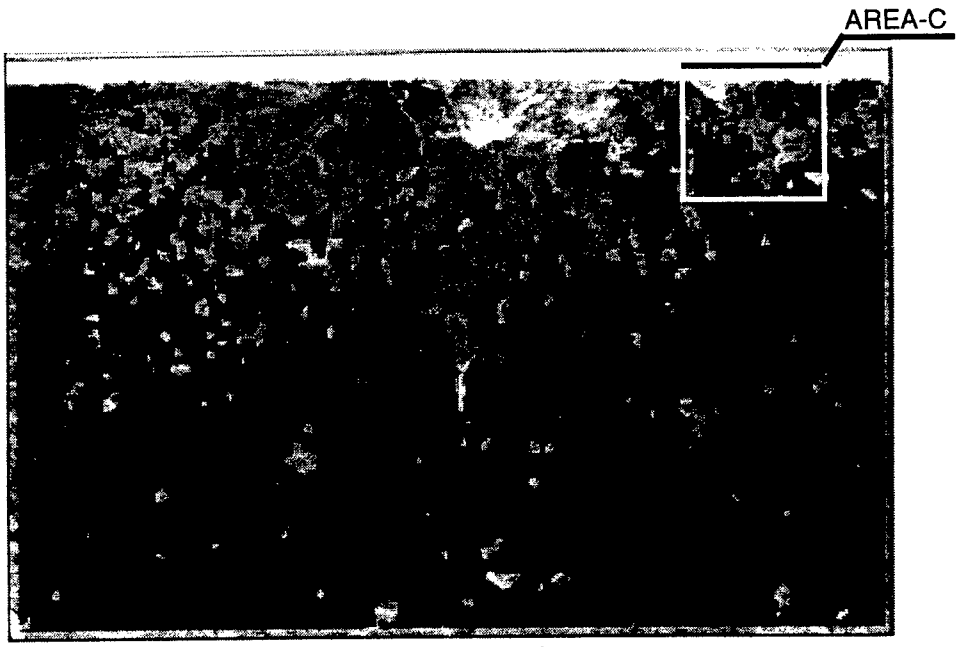

(e) FAPP at spacing of 0.556

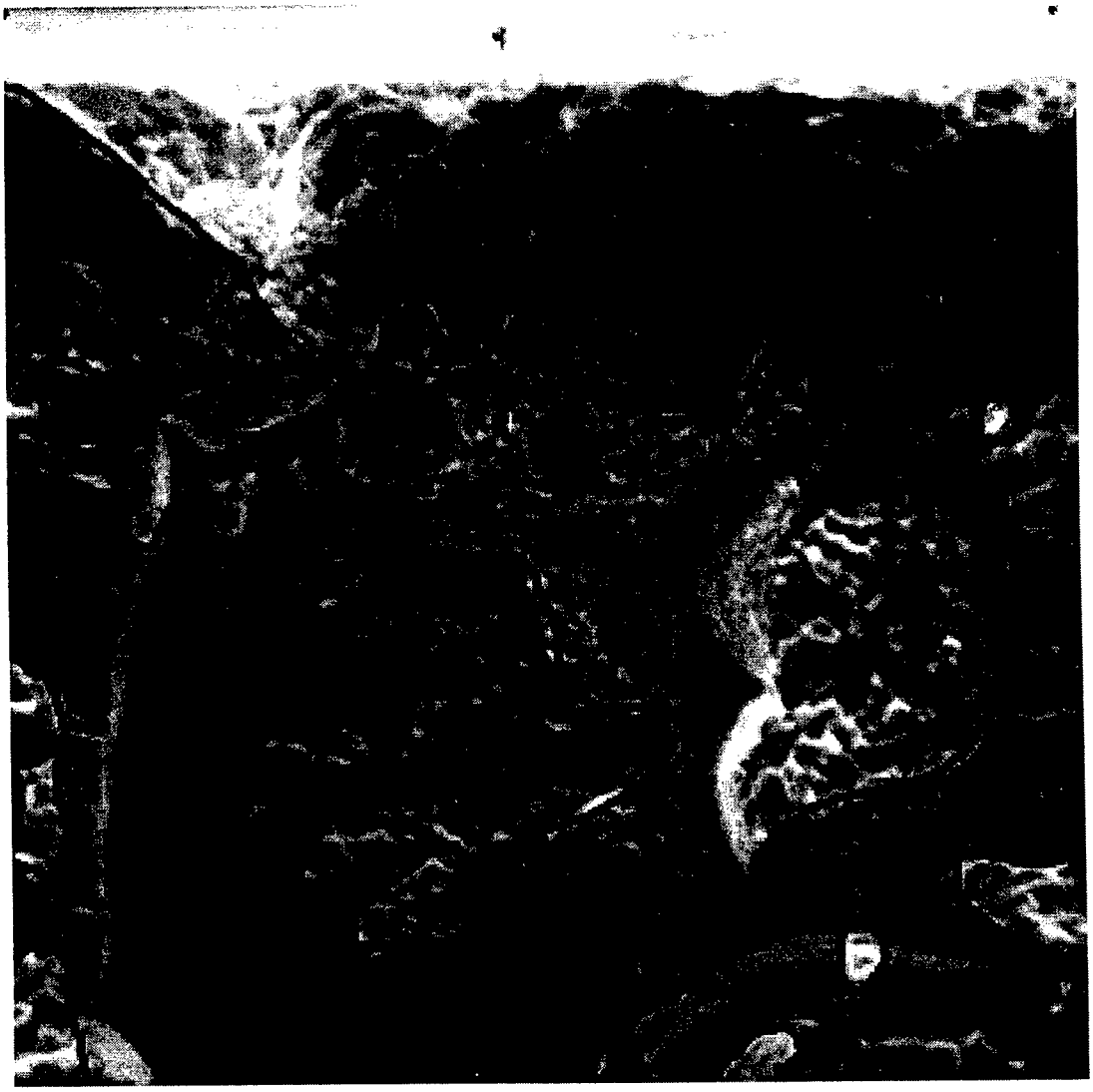

(f) Enlargement of Area-C

Figure 11. Early microfailure sites and fracture surface features (continued).

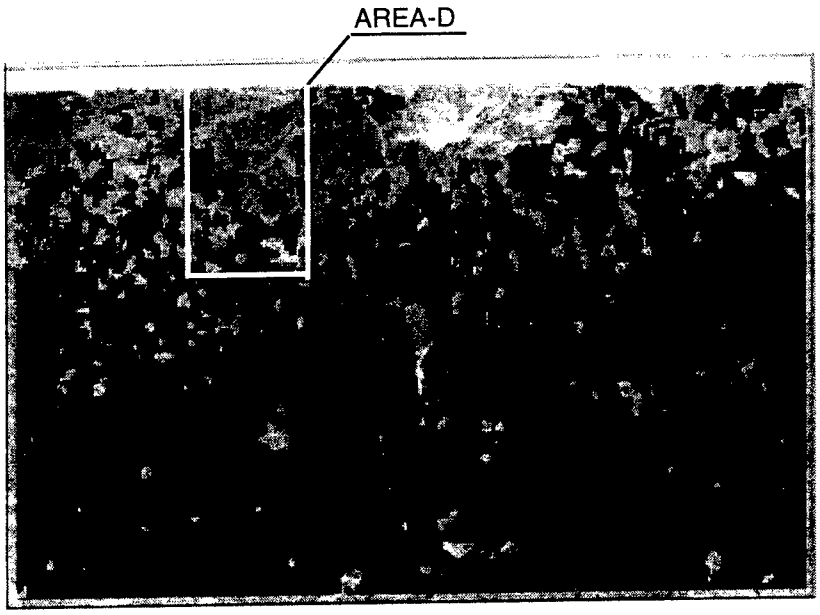

(g) FAPP at spacing of 0.556

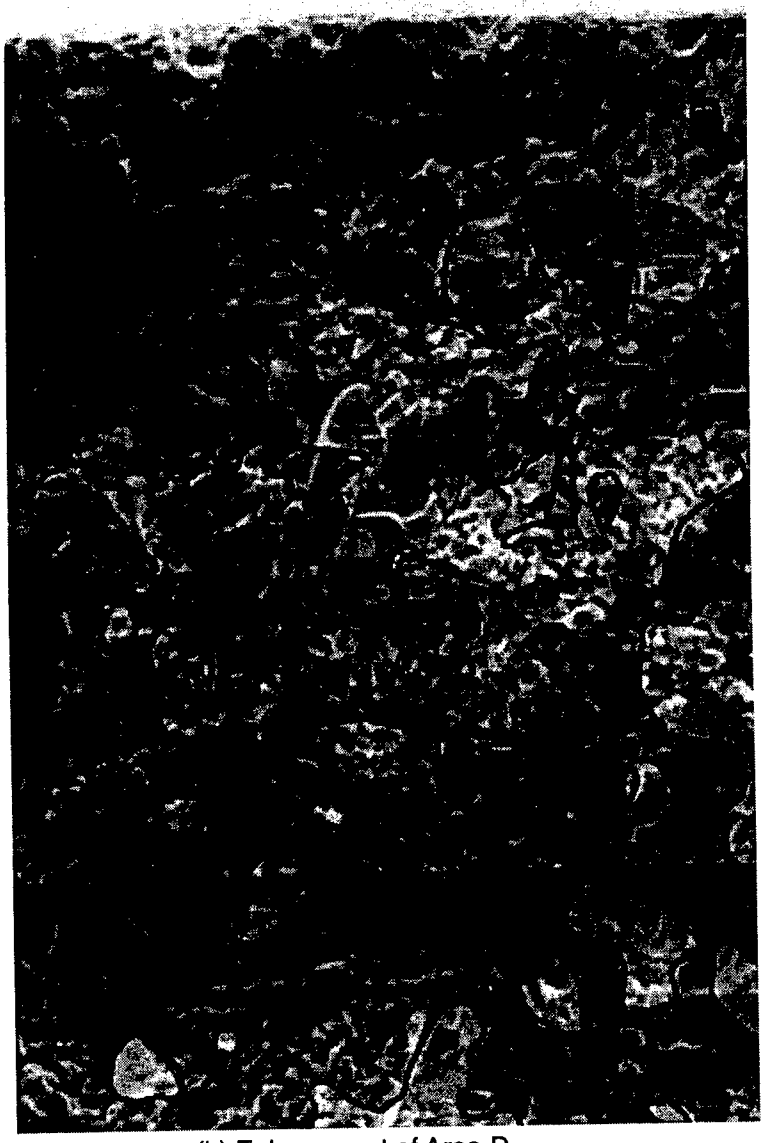

(h) Enlargement of Area-D

Figure 11. Early microfailure sites and fracture surface features (concluded).

earlier stage (i.e., at the separation of 0.532 shown in figure 11b). Figure 11d shows how debonded areas grow through the microstructure.

Figure 11e shows an area where rapid debonding was observed, and figure 11f is the enlargement of the framed area. Again, a correlation between early debond formation and agglomerate boundaries and triple points is obvious.

Figure 11g illustrates an area where coalescence of debonded areas occurred early. The closer look afforded by figure 11h shows agglomerates and agglomerate boundaries, but also differences in appearance of the failed area from the areas where microfailure did not occur. Although the causes of agglomerate debonding were not studied further, such a study would be interesting and worthwhile from a material development viewpoint.

DISCUSSION AND CONCLUSIONS

FRASTA was applied to pinpoint microfailure events in the interior of an alumina specimen under four-point-bend loading and determine the sequence of their occurrences. One objective was to correlate the local microfailure events with AE signals. However, because the number of microfailure events detected by FRASTA was about an order of magnitude larger than the number of AE events recorded by the transducer system, a one-to-one correlation required a way to identify those microfailure events that produced large AE signals. Attempts to pick out and correlate sudden microfailure nucleation, growth, and coalescence events were not successful.

FRASTA, however, identified general regions where the fracture surface rapidly developed and where many of the AE signals likely originated. Although the individual microfailure activity within these regions was discernible, the activity could not be tied to the AE spectra. Further research is required to determine which microfailure characteristics result in intense acoustic signals. Advanced, wide-band sensors that record the waveforms of AE's may provide the additional information (e.g., three-dimensional location) that allows individual AE signals to be assigned to specific microfailure events.

The FRASTA results showed that microfailures nucleate preferentially at agglomerate boundary triple points and grow preferentially on agglomerate boundary surfaces. Consequently, the macrocrack that eventually forms has a diffuse, rather poorly defined front.

The ability of FRASTA to reconstruct detailed descriptions of microfailures and relate microfailure evolution to microstructure should find use in failure analysis and in the development

of advanced ceramics. Microstructural causes of the weakness in the material can be quickly determined, and thus considerable time and effort can be saved in developing new materials.

Finally, this work demonstrated how FRASTA can assist in the application of fracture mechanics to ceramics. Determining the critical crack size at the point of failure is vital but often difficult. FRASTA provided the size and shape of the macrocrack at the time of unstable propagation, even though the fracture surfaces appeared unmarked when examined with an SEM and the crack front was diffuse.

CHAPTER 2: ACOUSTIC EMISSION SOURCES IN WELDED BRIDGE STEEL DEDUCED FROM FRACTURE SURFACE TOPOGRAPHY ANALYSIS (FRASTA)

Microfailure origins of acoustic emission (AE) were sought in a weldment of A36 bridge steel. A circumferentially notched and fatigue-precracked round bar tensile specimen was monotonically loaded to failure at 0 °C. Ten AE signals emanating from the fracture plane were recorded. The sites and sequence of microfailures were determined from the fracture surface topography using the FRASTA technique.

The first three AE signals correlated with microfailures near the fatigue precrack front; the later signals emanated from the specimen interior where microfailure sites could not be pinpointed on the fracture surfaces. Each of the three identifiable microfailure initiation sites consisted of a field of fine dimples; however, a small area of cleavage existed in two sites, suggesting that acoustic signals are produced by brittle cleavage of certain grains in the steel microstructure. Supporting evidence was provided by a similar fracture test conducted at room temperature, in which the specimen failed entirely by ductile void evolution and emitted no detectable AE.

BACKGROUND

The acoustic energy emitted by a failing material as microcracks form, grow, and coalesce can often be detected by in-contact transducers. Therefore, acoustic signals could provide advance warning of impending unstable crack growth and structural collapse. The phenomenon is the basis for a nondestructive evaluation technique currently applied in materials and failure research, as well as in proof testing of structures, such as pressure vessels.[8]

Acoustic emission is attractive as a means to monitor the integrity of aging structures such as bridges.[9,10] As opposed to visual or ultrasonic inspections that must be performed periodically, AE monitoring is continuous and is not labor intensive. For AE monitoring to be practical, however, several current shortcomings must be overcome. A way must be found to discriminate relevant from irrelevant signals. Particularly important in bridge applications is a way to distinguish between signals produced by microcracking events occurring within a bridge member, and extraneous signals, emanating, for example, from fretting and impact produced by bridge traffic and wind loading. A way is also required to interpret, at distances remote from the

crack, sound waves that have undergone reflections and mode transformations in traveling through a complex geometry from crack to transducer. A way is also needed to manage the large amount of data generated by continuous monitoring.

The Federal Highway Administration is addressing these shortcomings in a research program that includes efforts to develop a high-fidelity broad band sensor and a high digital bandwidth signal acquisition and storage system, to model and computationally simulate far field signal propagation, and to link microstructural failure events with AE signals. The program is summarized in reference 1.

This section reports on the effort to establish relationships between acoustic emission signals and the microfailure events that caused them. The approach was to perform tensile tests on a bridge steel weldment in the laboratory, monitor the acoustic emission with resonant frequency sensors, analyze the resulting conjugate fracture surfaces to determine the sequence of microfailure events, and correlate the microfailure events with the AE record. Key to success is a fractographic technique, FRASTA, that permits reconstruction of the failure process in microscopic detail. The technique pinpoints the sites of microfailure and delineates the sequence of microfailure events, thus allowing individual microfailure events to be correlated one-to-one with individual AE signals. The FRASTA procedure is described in the appendix.

SPECIMEN MATERIAL AND FRACTURE TEST

The specimen material was provided by the Federal Highway Administration in the form of a machined compact tension (CT) specimen of A36 steel containing an electroslag weldment in the midsection of the sample. Further details regarding composition, thermomechanical treatment, and welding conditions were unavailable.

A circumferentially fatigue-precracked, round-bar tensile specimen, figure 12, was tested to enhance the probability of producing detectable AE and to reduce the source region for relevant signals. This geometry provides a high level of three-dimensional constraint along the crack front and thus promotes local brittle behavior in the vicinity of the crack front, and hence AE.[11] Furthermore, the geometry tends to restrict microcracking to a small region, namely, the plane of the fatigue crack.

A notched round-bar tensile specimen was machined from the CT specimen so that the plane of the notch lay in the midplane of the weldment. The fatigue precrack was introduced at the notch root using a rotating fatigue technique in which the specimen was mounted in a lathe and

loaded transversely in four-point-bending. The applied 1000-N load produced a notch tip stress intensity of about 20 MPa$\sqrt{m}$. The resulting fatigue crack was concentric, and the average precrack depth was about 4.7 mm, resulting in a ratio of crack depth to specimen radius (a/R) of 0.59.

Specimen elongation was measured in a 50.8-mm gauge length by two diametrically opposed extensometers straddling the crack plane. Use of two extensometers allowed detection of eccentric loading and a way to minimize it by adjusting the specimen mounting in the loading jig. A load cell located in the machine load train recorded the load history.

Two piezoelectric resonant-type AE sensors (Physical Acoustics Corporation Model No. R-15) were coupled to the specimen surface symmetrically 10 mm above and below the crack plane using aluminum alloy waveguides, as shown in figure 12. A Physical Acoustics Corporation Locan 320 work station was used to record AE signals during the test. Output signals from the AE sensors were amplified 40 dB at the preamplifier and an additional 30 dB at the amplifier. Signals with amplitudes less than 45 dB were rejected during the test. After the test, the times of arrival of signals from each AE sensor were compared, and events with different times of arrival were rejected as originating outside the crack plane. The valid AE signals were correlated with the load and elongation records.

The specimen was fractured under a monotonically increasing load in a servohydraulic testing machine using the actuator displacement as the control signal. A displacement rate of 0.25 mm/min yielded an elastic loading rate of 5 kN/min. An initial test performed at room temperature did not produce detectable AE signals from the plane of fracture. Therefore, a second fracture test was conducted at 0 °C to encourage brittle behavior and localized microcracking. This test resulted in 10 AE events before the specimen ruptured.

Figure 13 shows the plot of applied load versus average displacement at the crack plane and the locations on the curve where the AE signals were recorded. An average displacement at the crack plane was computed by subtracting the elastic deformation occurring away from the notched region from the specimen elongation data, and was used to directly compare the results with the FRASTA results. As shown in the figure, the overall crack plane displacement before rupture was 84 μm. AE signals observed during the test are indicated on the curve (the last two circles in figure 13 represent two AE events each); the displacement from the first recorded AE signal to the rupture point was 46 μm.

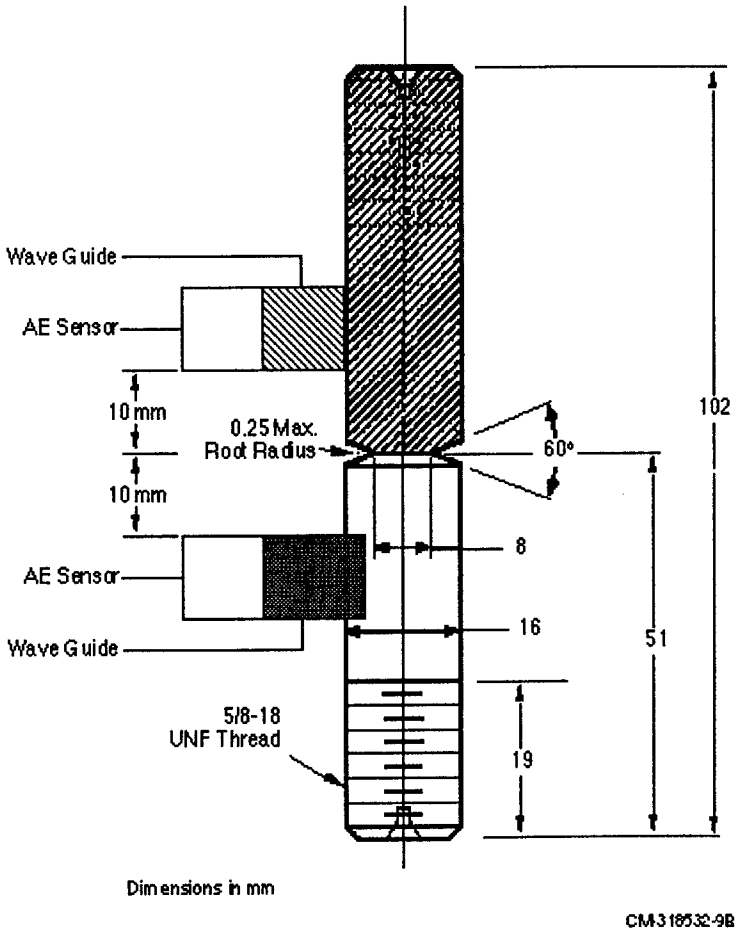

Figure 12. Geometry and dimensions of notched round bar specimen with AE sensors and wave guides.

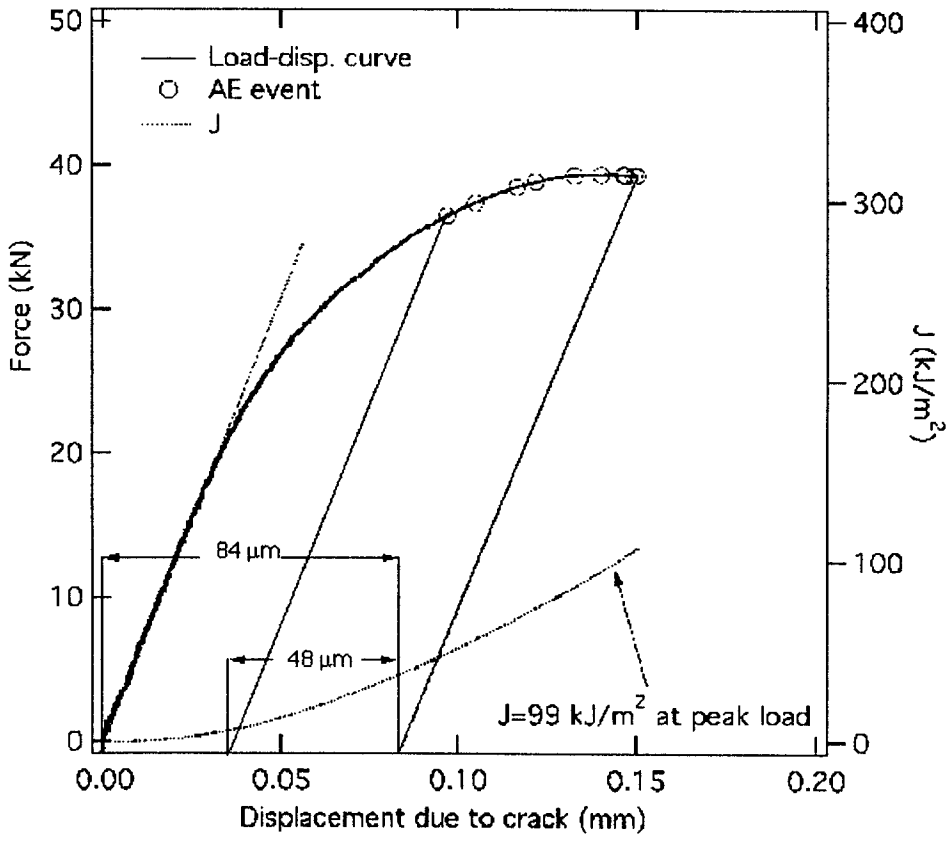

Figure 13. Load versus average crack face displacement. AE events are indicated. (The last two open circules represent two AE events each.)

FRACTOGRAPHIC ANALYSIS

The SEM photographs of the conjugate fracture surfaces, figure 14, show a large ridge (1.6 mm high), suggesting that two macrocracks propagated from opposite sides of the specimen and intersected on different planes to rupture the specimen. The surface features reflect the mixed and complex microstructure of the weld metal. For example, the grain axes of the material in this section of the test specimen appear to be oriented from the top right corner to the bottom left corner, as evidenced by the texture of the fracture surface as well as the fatigue precracked area. Patches of smooth fracture areas are evident at several locations near the circumferential fatigue precrack front. Higher magnification examination revealed the fracture mechanism of these areas to be void nucleation, growth, and coalescence. The interior fracture surface was predominantly cleavage.

To delineate the sources of the acoustic emission recorded during the fracture test, we sought to reconstruct the microfracture process by applying FRASTA to the fracture surfaces. The topography of each fracture surface was quantified by a scanning confocal lens laser microscope, then the conjugate topographs were juxtaposed to correspond to the relative positions of the conjugate fracture surfaces during specimen loading and rupture. By analysis of the misregistries of the fracture surface topographs at increasing relative displacements, the sites and sequence of microfailure nucleation and the growth and coalescence of nucleated microfailures could be identified and studied.

Figure 15 shows the gray-scale topography images of the surfaces in figure 14. White areas in the image represent higher elevation and dark areas lower elevation. These images clearly indicated the large ridge evident in figure 14. The digital data of the conjugate surfaces were used to reconstruct the fracture process. Figure 16 shows a series of fractured area projection plots (FAPP's), i.e., plan views normal to the tensile axis in which black areas are areas where the topographs overlap and white areas are nonoverlap areas. The white areas are interpreted to be microfailures and black areas to be intact material. Viewed successively, the FAPP's at increasing spacings portray the development of the fracture surface. Isolated white dots on black fields (in the early plots) and black dots on white fields (in the later plots) are noise in the system resulting from resolution limitations. Thus the failure evolution evaluation must be done keeping background noise in mind.

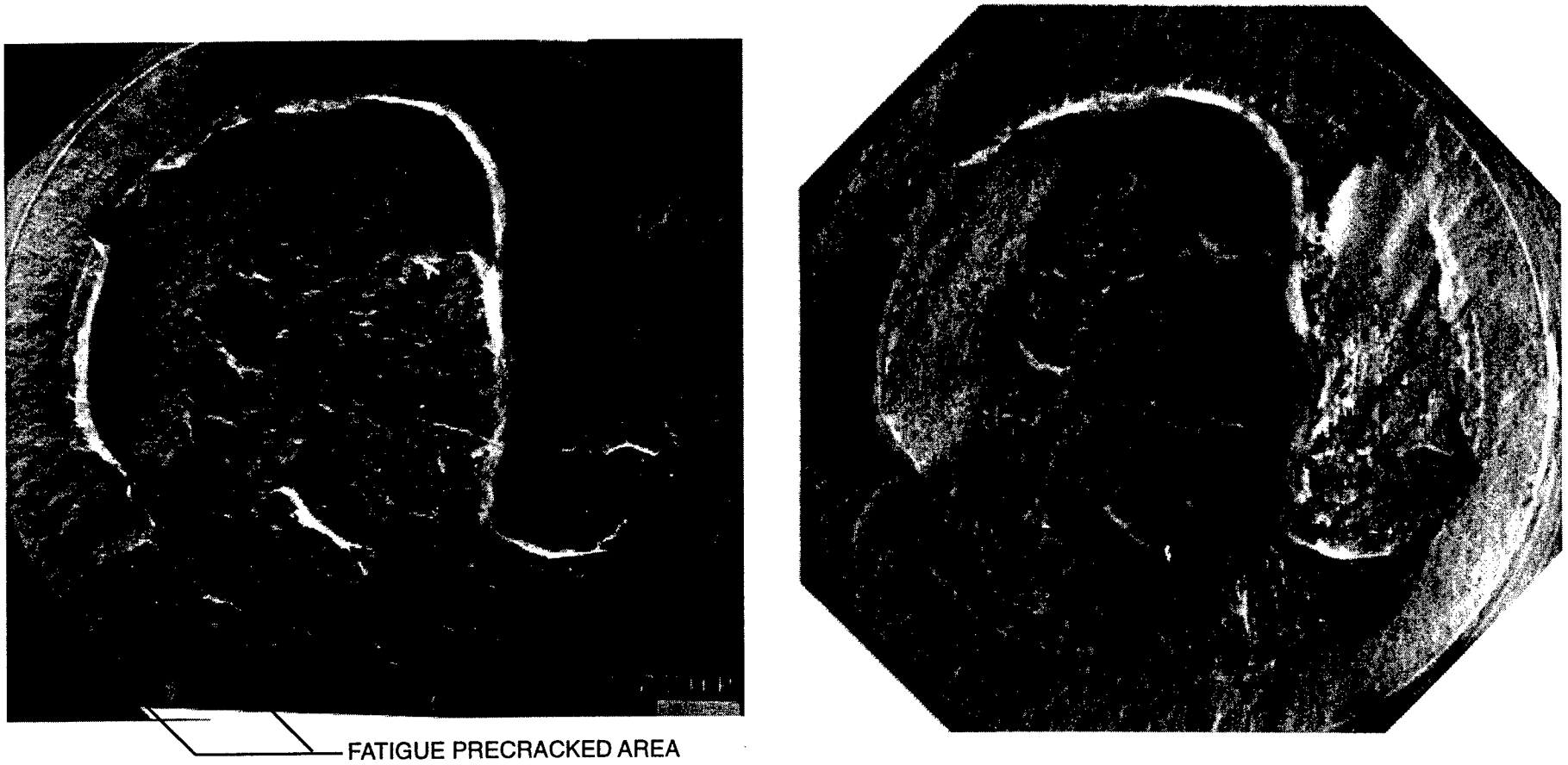

(a) Surface A

(b) Surface B (Horizontally Flipped)

Figure 14. SEM photographs of conjugate fracture surfaces. (The image of Surface B was flipped horizontally to allow easy comparison of features with Surface A.)

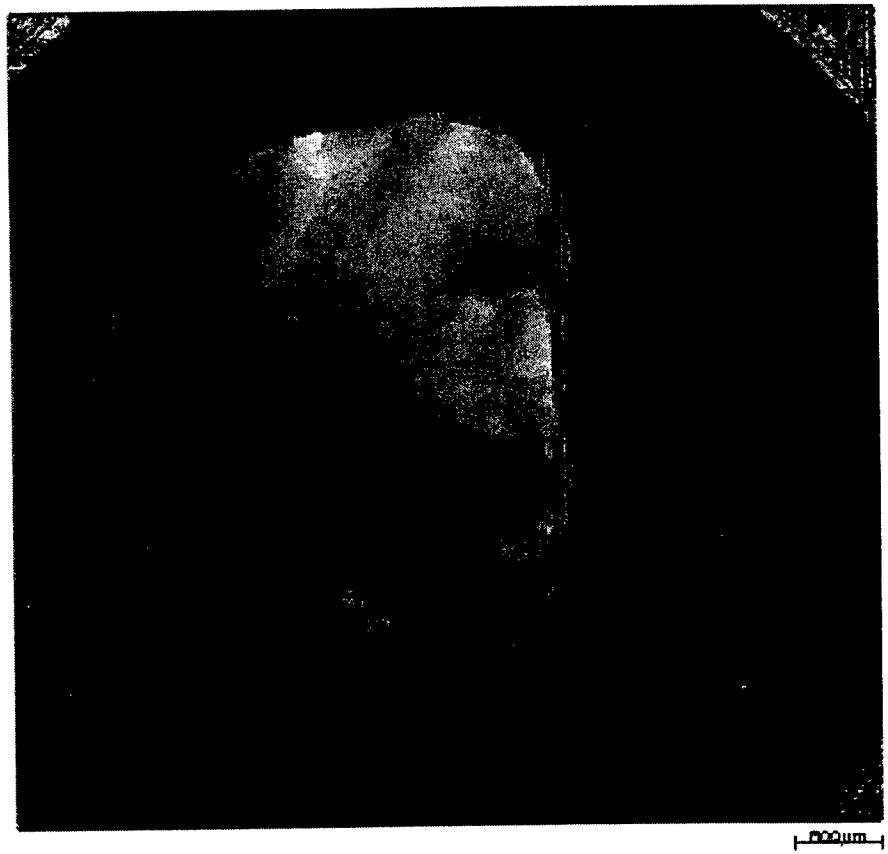

(a) Gray-Scale Topography Image of Surface A

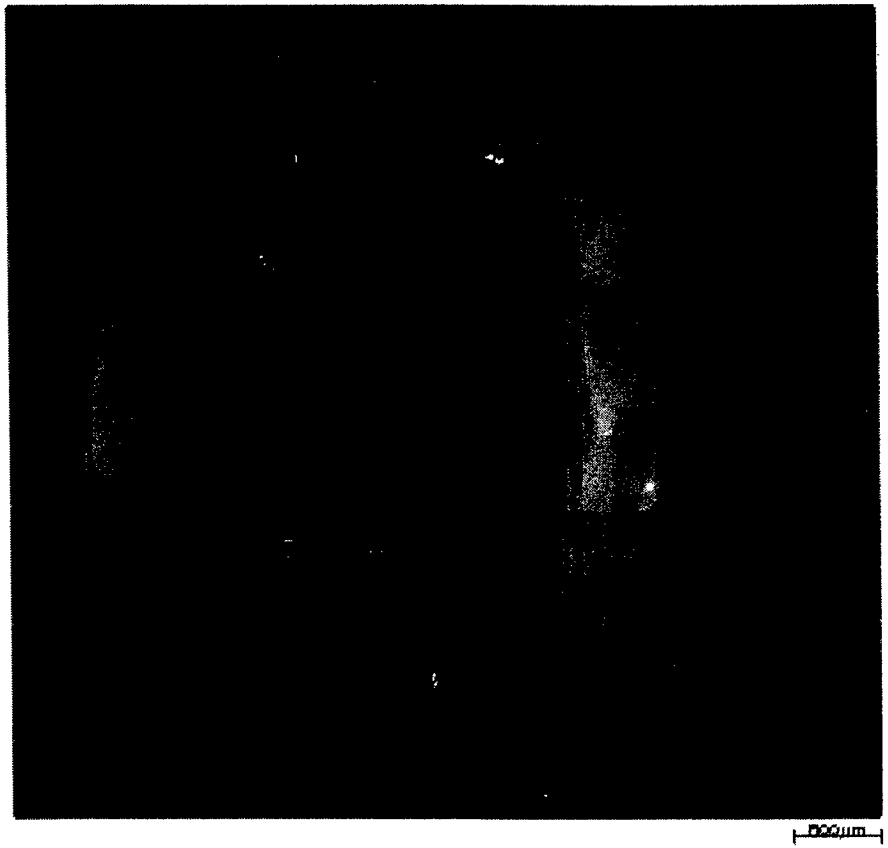

(b) Gray-Scale Topography Image of Surface B

Figure 15. Gray-scale topography images of conjugate fracture surfaces of circumferentially fatigue-cracked tensile specimen. (Surface B image was flipped horizontally to allow easy comparison with Surface A.)

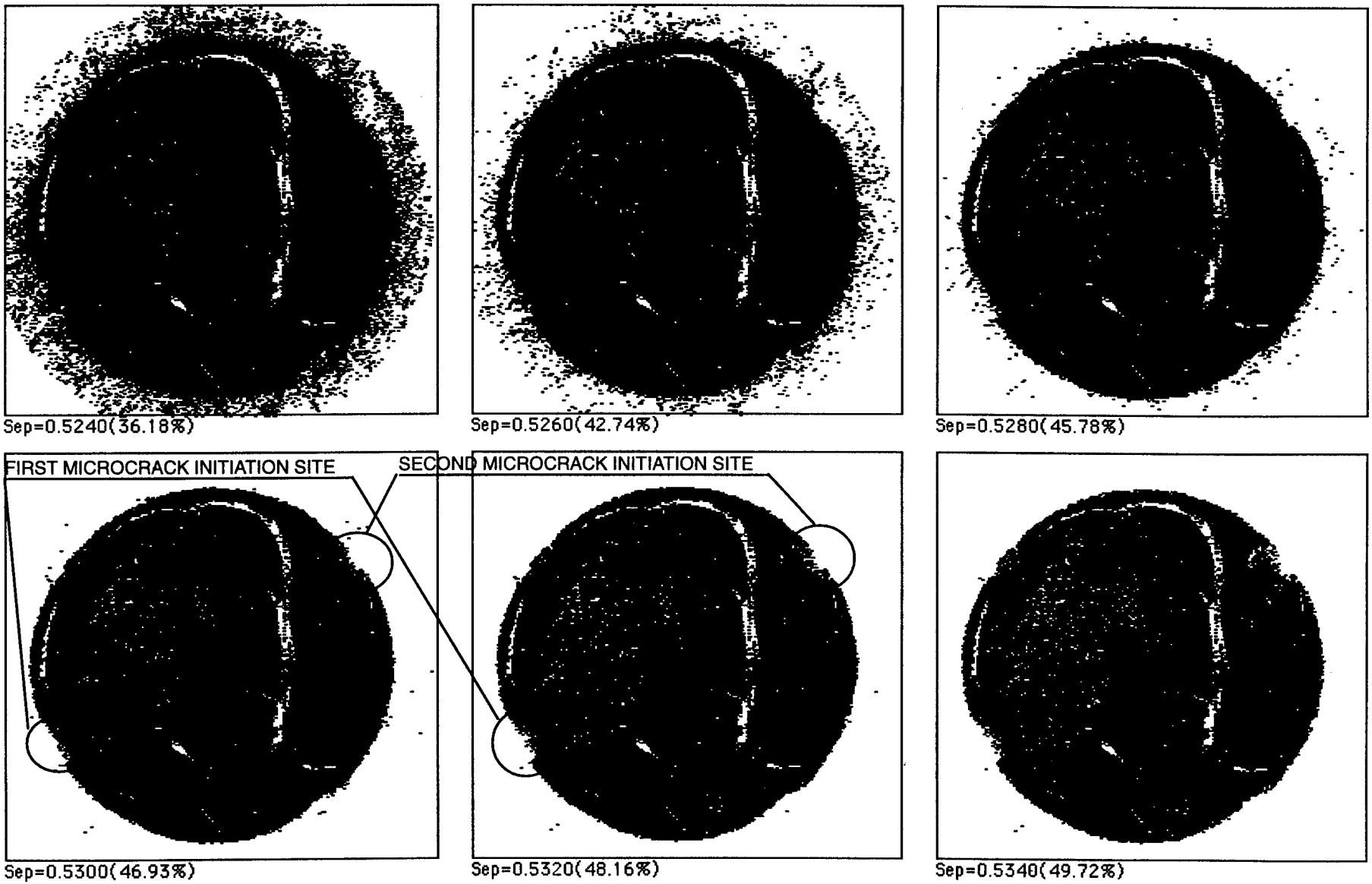

Figure 16. A series of FAPP's showing the microfracture processes in the circumferentially fatigue-precracked tensile specimen. (White areas indicate material separation; black areas indicate intact material. Random white dots are noise.)

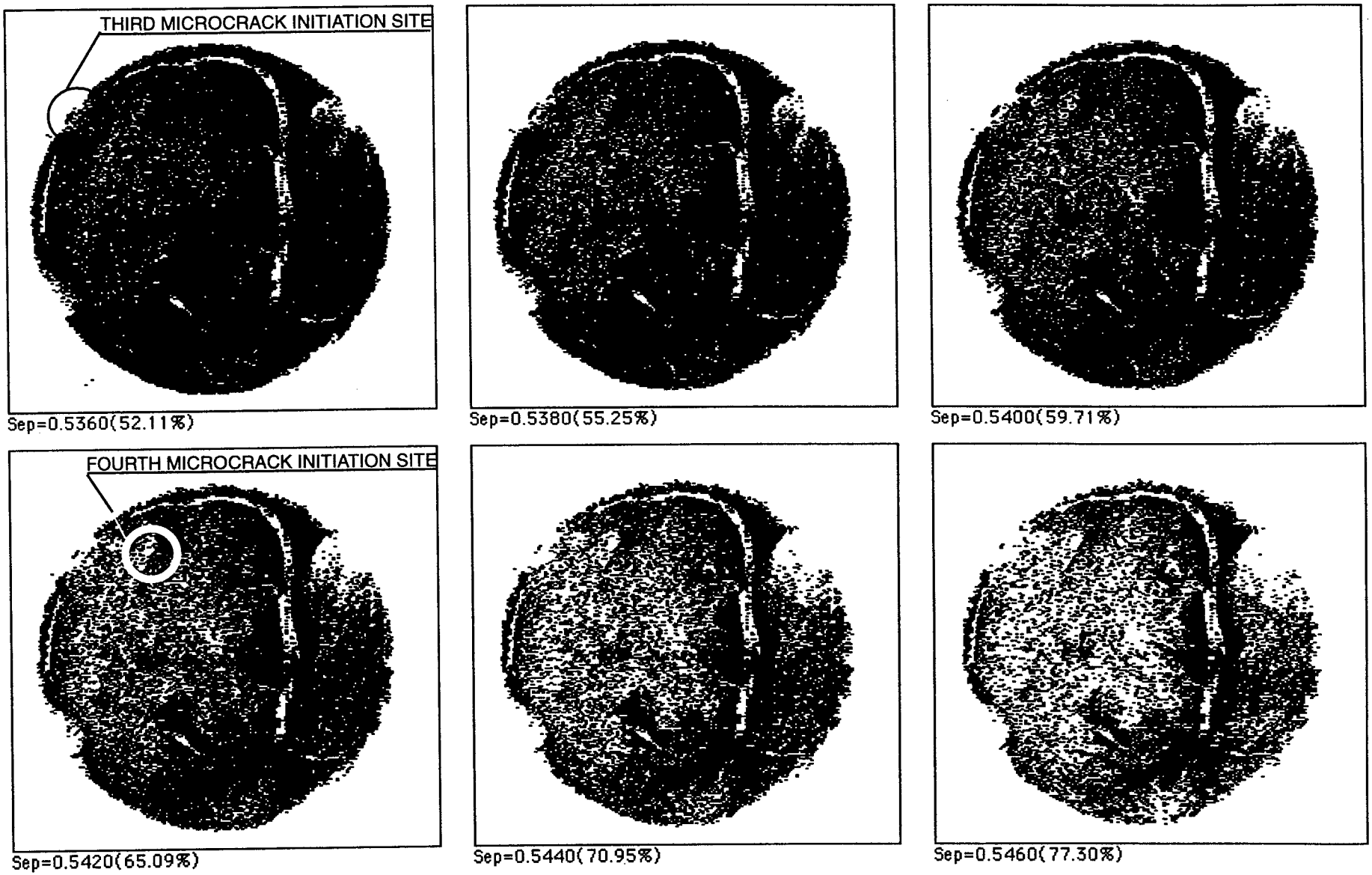

Figure 16. A series of FAPP's showing the microfracture processes in the circumferentially fatigue-precracked tensile specimen (concluded). (White areas indicate material separation; black areas indicate intact material. Random white dots are noise.)

The first microcracks (the white areas at 2 o'clock and 8 o'clock on the fatigue precrack front) appear in the plot at the spacing of 0.530. (Actual initiation appears to occur somewhat earlier, but the fracture increase rate shown in figure 17 and the AE record suggests rapid microfailure at a spacing of 0.531.) Later plots portray the growth of these cracks and the formation of a third crack at 11 o'clock on the precrack front at the spacing of 0.536. At larger spacings additional microcracks form in the specimen interior; however, these were poorly resolved in the FAPP's. A fourth microcrack is speculated to form in the interior near the third crack at a spacing of 0.542. Material near the large fracture surface ridge was the last to fail.

The relative rate of specimen fracture during the monotonic load application was obtained by plotting the fractured area (percentage of white area) in each plot as a function of conjugate surface spacing, figure 17. At spacings below 0.5248, the slope is steep. This range represents the fatigue-precracking stage where crack growth was accompanied by only a small amount of inelastic deformation. Between the spacings of 0.5248 and 0.5307, the fractured area increase slowed, indicating plastic blunting of the fatigue crack tip. The small linear slope between 0.527 and 0.530 indicates true cracktip blunting behavior; the range between 0.524 and 0.527 represents the transition from fatigue to monotonic loading.

At the spacing of 0.5307, a deviation from the linear relationship occurred, indicating crack formation at the fatigue precrack front. The fractured area increase rate gradually and continuously accelerated up to 0.5428, beyond which the slope again became linear. This suggests that the crack became unstable at the spacing of 0.5428, and rapid crack growth occurred. The fracture surface displacement from formation of the first microcrack (0.5307) to the moment of crack instability (0.5428) was 46 μm. This displacement agrees well with the crack surface displacement from the first AE signal to final rupture (48 μm) as measured on the specimen with the extensometers and shown in figure 13.

Assuming the first acoustic emission occurred at a conjugate surface spacing of 0.5307, the conjugate surface spacings that corresponded to the later AE signals were calculated and the corresponding FAPP's constructed. These FAPP's were then superimposed over the SEM photograph of the fracture surface to identify the sites and boundaries of the microfailures. Figure 18a shows the SEM photograph of figure 14, and Figure 18b shows the photograph with the FAPP at the spacing of 0.5307 superimposed. The local area of the fracture surface that failed first is indicated.

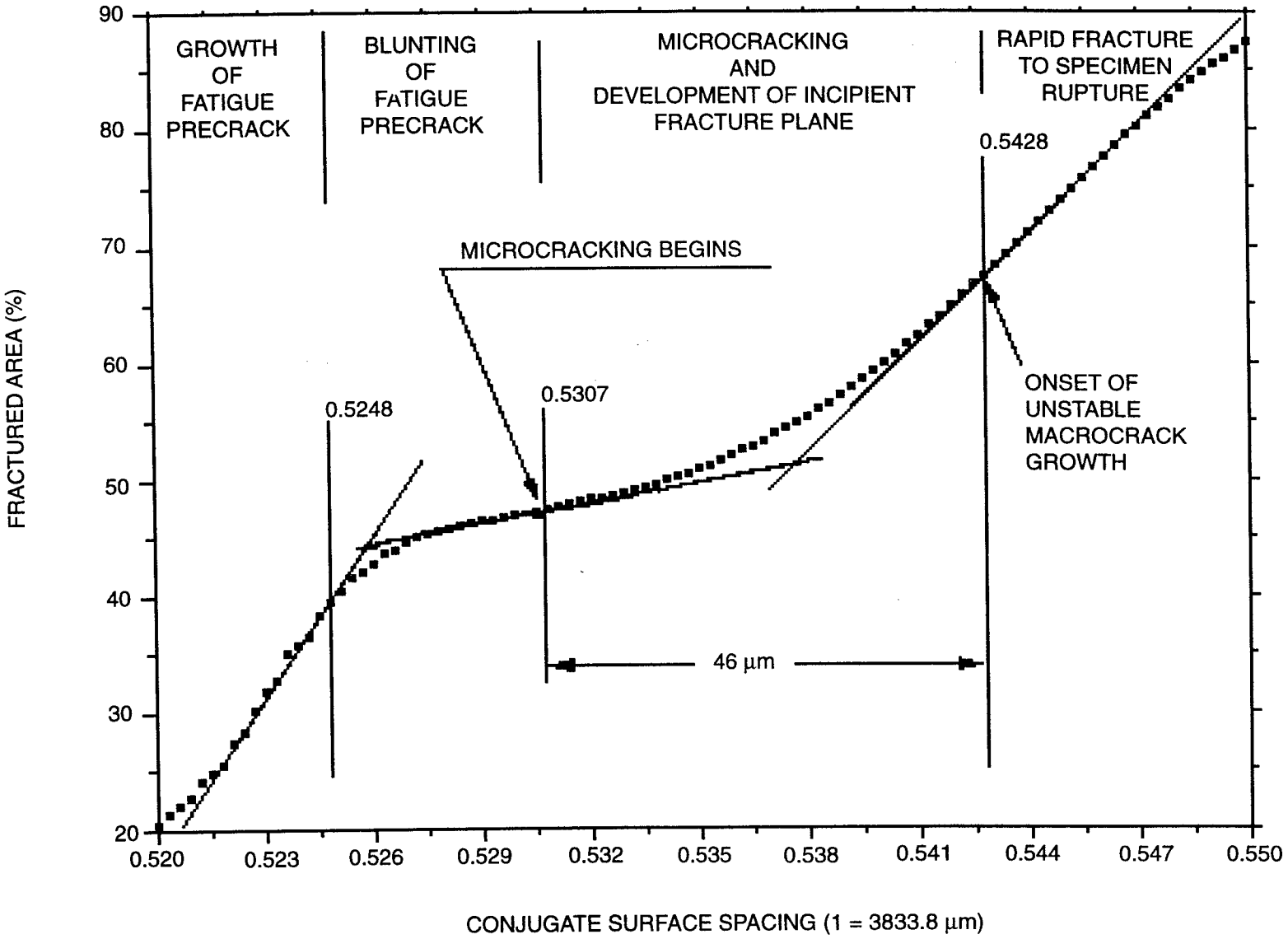

Figure 17. Fractured area increase as a function of conjugate surface spacing.

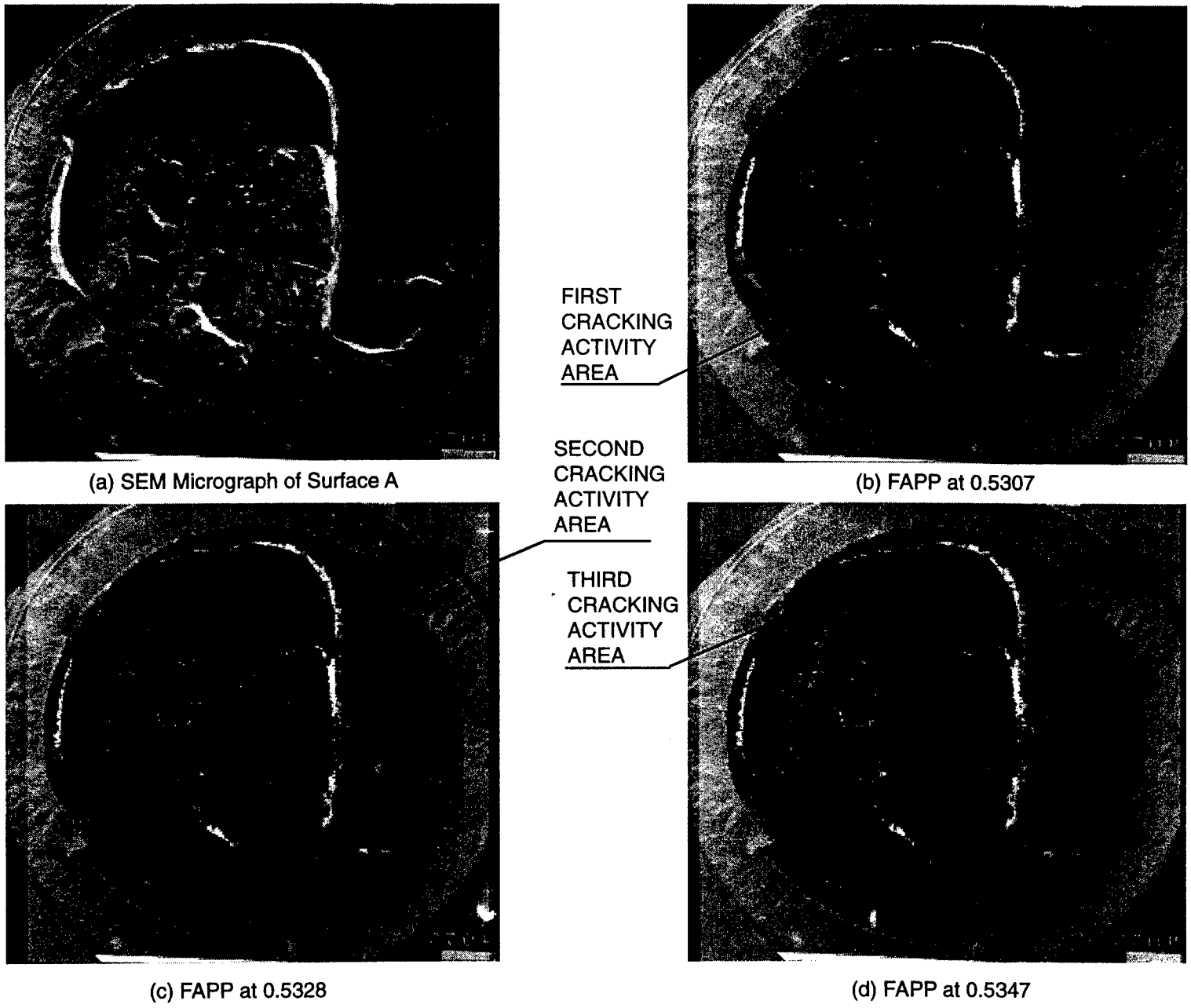

Figure 18. Superposition of FAPP's at various topograph spacings on the SEM photograph of the fracture surface.

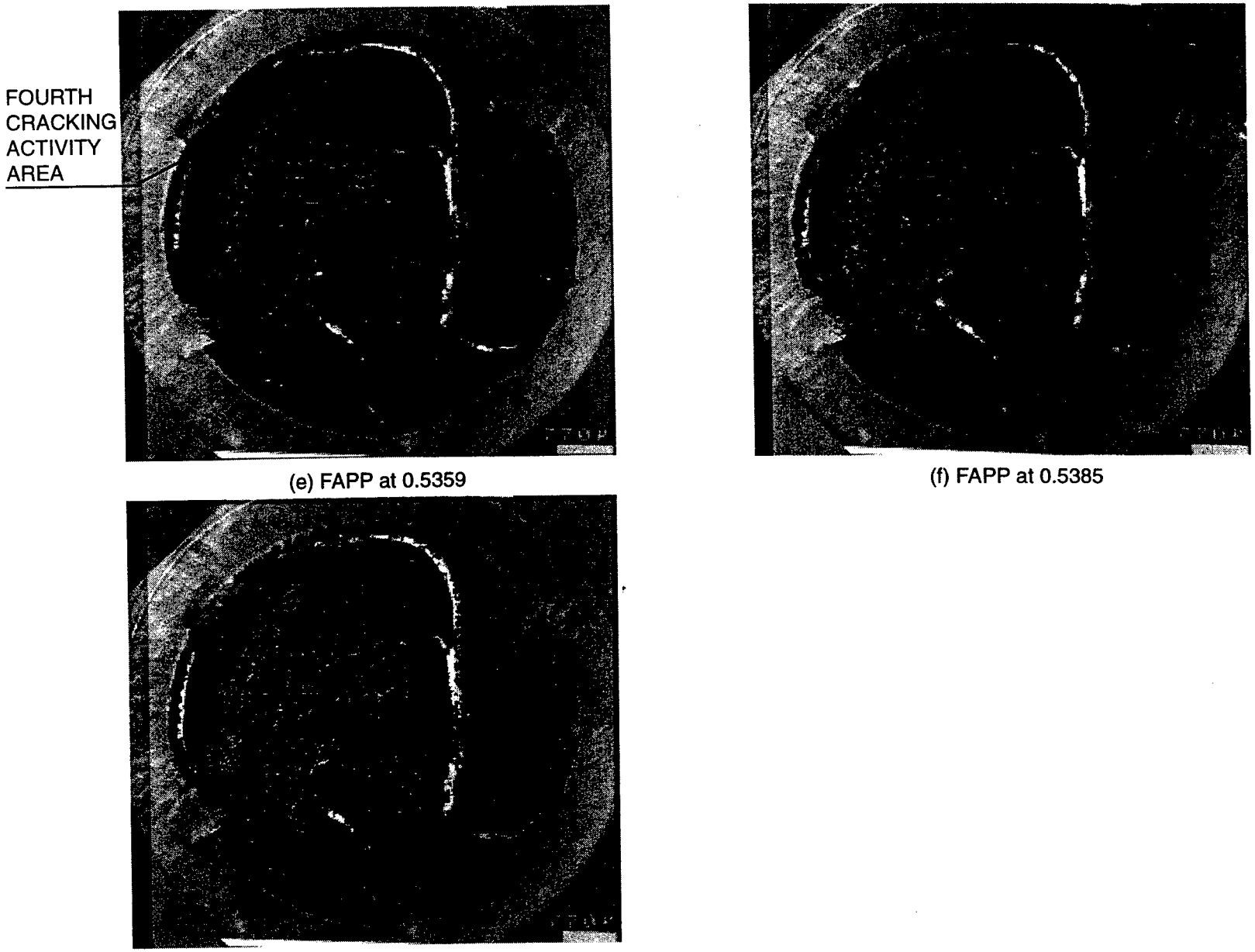

Figure 18. Superposition of FAPP's at various topograph spacings on the SEM photograph of the fracture surface (concluded).

Figure 19 shows a higher magnification SEM photograph of the area at 8 o'clock, revealing that the fatigue precrack front bisected a large grain and that void nucleation and growth are the failure mechanisms of the remainder of the grain. However, tiny areas of brittle cleavage exist at locations A and B within the dimpled failure site. Enlargements of these local areas are shown in figures 19b and 19c. These cleaved areas could be possible sources of acoustic emission.

Figure 18c shows a composite of the SEM image and FAPP at the spacing of 0.5328 that corresponded to the state of fracture at the time of the second AE signal. The FAPP indicated the formation of the second microcrack at two o'clock on the fatigue precrack front. Again this area is characterized by a large grain that is bisected by the fatigue precrack front. A higher resolution photograph of this area, figure 20a, shows the main fracture mechanism to be void nucleation and growth. FRASTA indicated that this microfailure initiated in area A; however, there exist no special features such as cleavage facets in this area that might be expected to produce an acoustic signal. Although an island of brittle fracture was observed at B, this area fractured later.

Figure 18d shows the FAPP corresponding to the deformation state when the third AE event occurred. The figure shows that the previous two cracks grew larger, and that a new crack formed at 11 o'clock. A high resolution SEM micrograph of this area, figure 21, shows the predominant fracture mechanism to be void nucleation and growth. FRASTA predicted the crack initiation site to be in the area marked A and figure 21b is the enlargement of this area. An island of brittle fracture is observed in the middle of the dimpled field and is possibly the source of the third AE signal.

Figure 18e shows the SEM micrograph superimposed by the FAPP at 0.5359, which portrays the deformation state at which the fourth AE signal was detected. At this stage we observe formation of internal cracks. Although the FAPP does not clearly indicate the site of crack formation, the later FAPP's (figures 18f and 18g) suggest that the area marked is the site of crack formation. Figure 22 provides a higher magnification view of this area. Examination of figures 14 and 22 indicates that the microstructure at this location is coarse and that the failure mode is brittle. Figure 22b shows an enlargement of area A in figure 22a, revealing a cleavage type failure surface.

Figures 18f and 18g show the state of fracture at later times. No microfailure sites are clearly defined, so correlations with the AE signals was not possible.

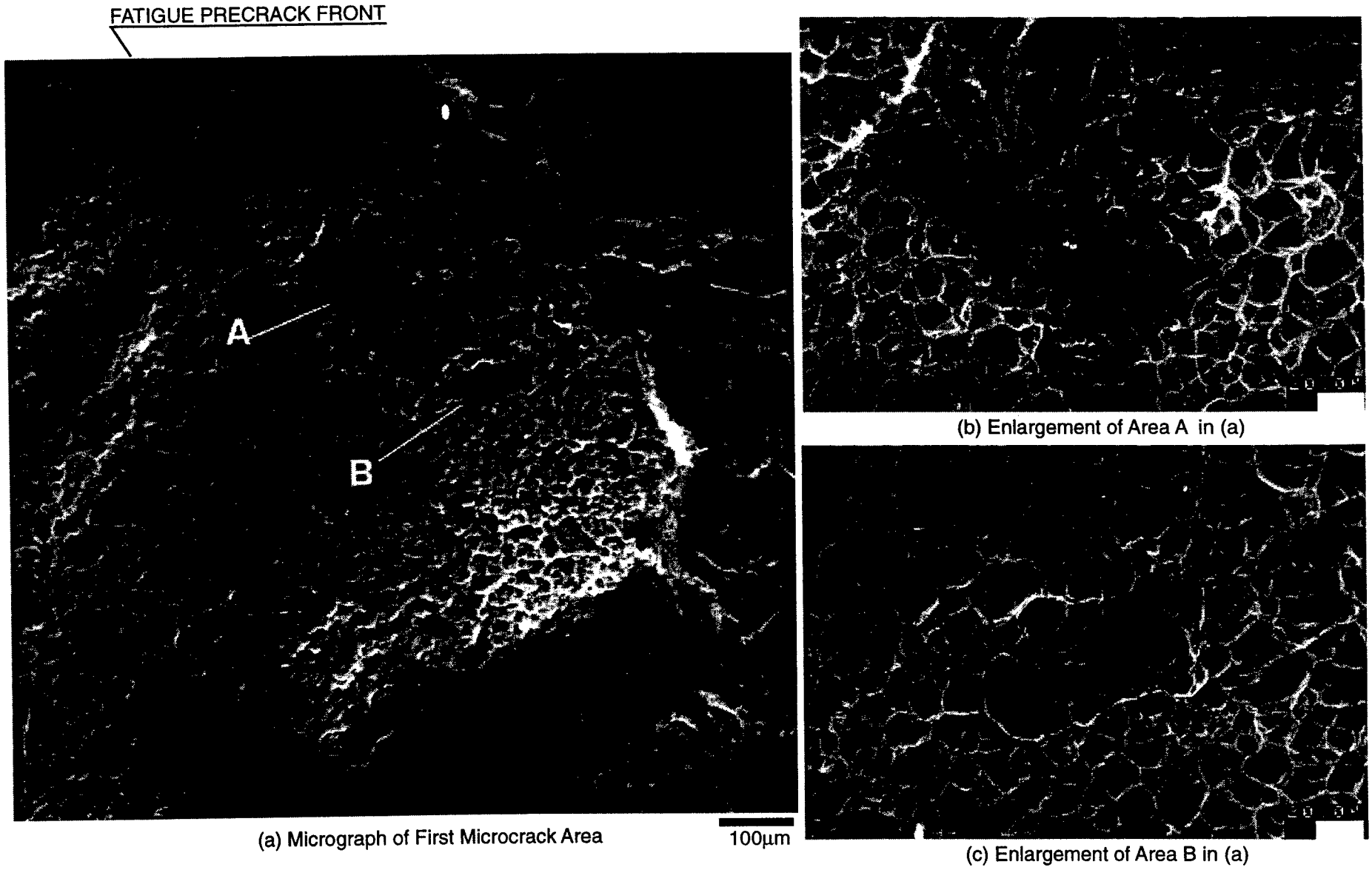

Figure 19. SEM micrographs of the area where FRASTA detected first microcrack formation.

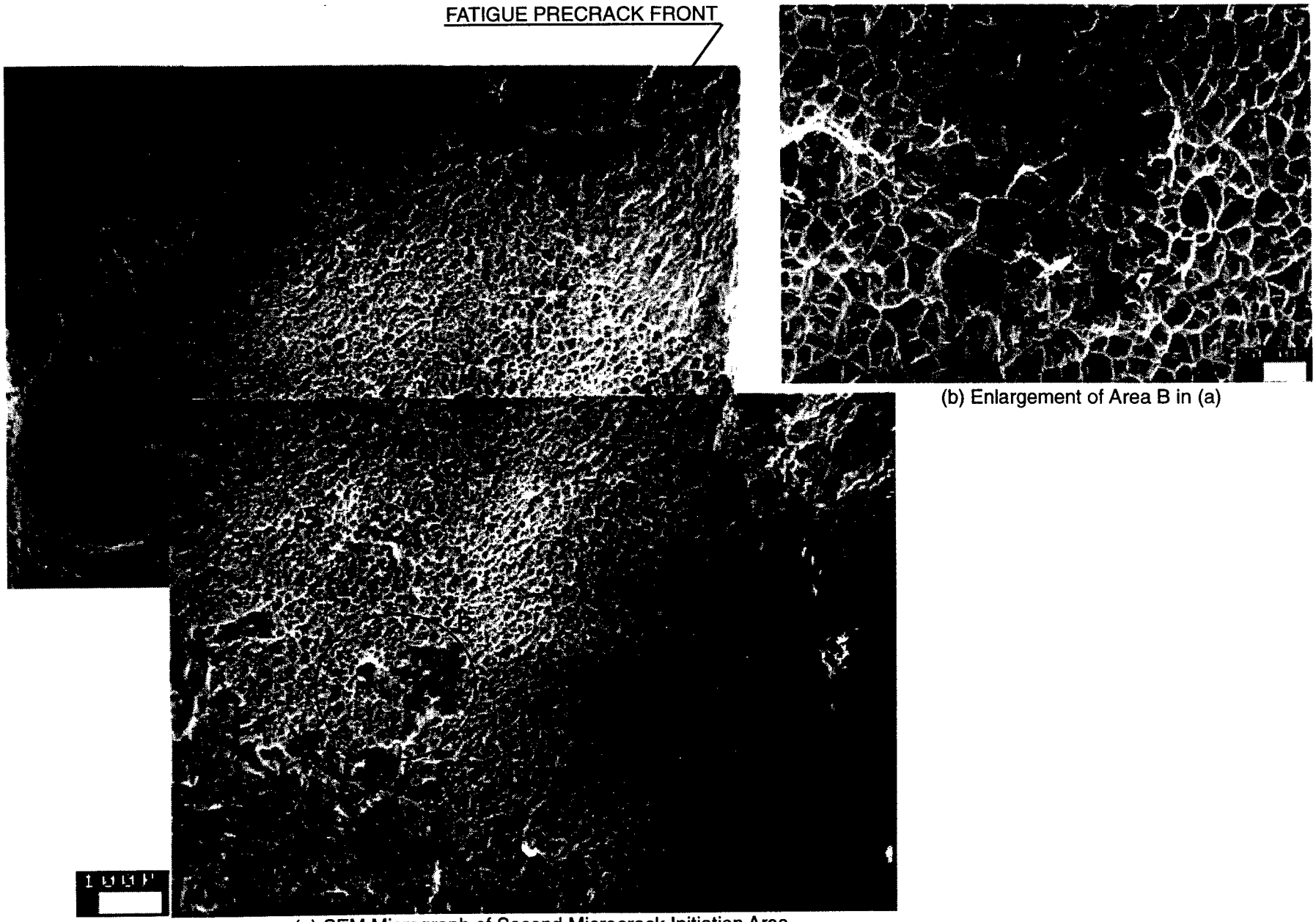

(b) Enlargement of Area B in (a)

(a) SEM Micrograph of Second Microcrack Initiation Area

Figure 20. SEM micrograph of the area where FRASTA detected second microcrack formation. (Area A is the site of microcrack formation, but brittle fracture facets were also observed at area B.)

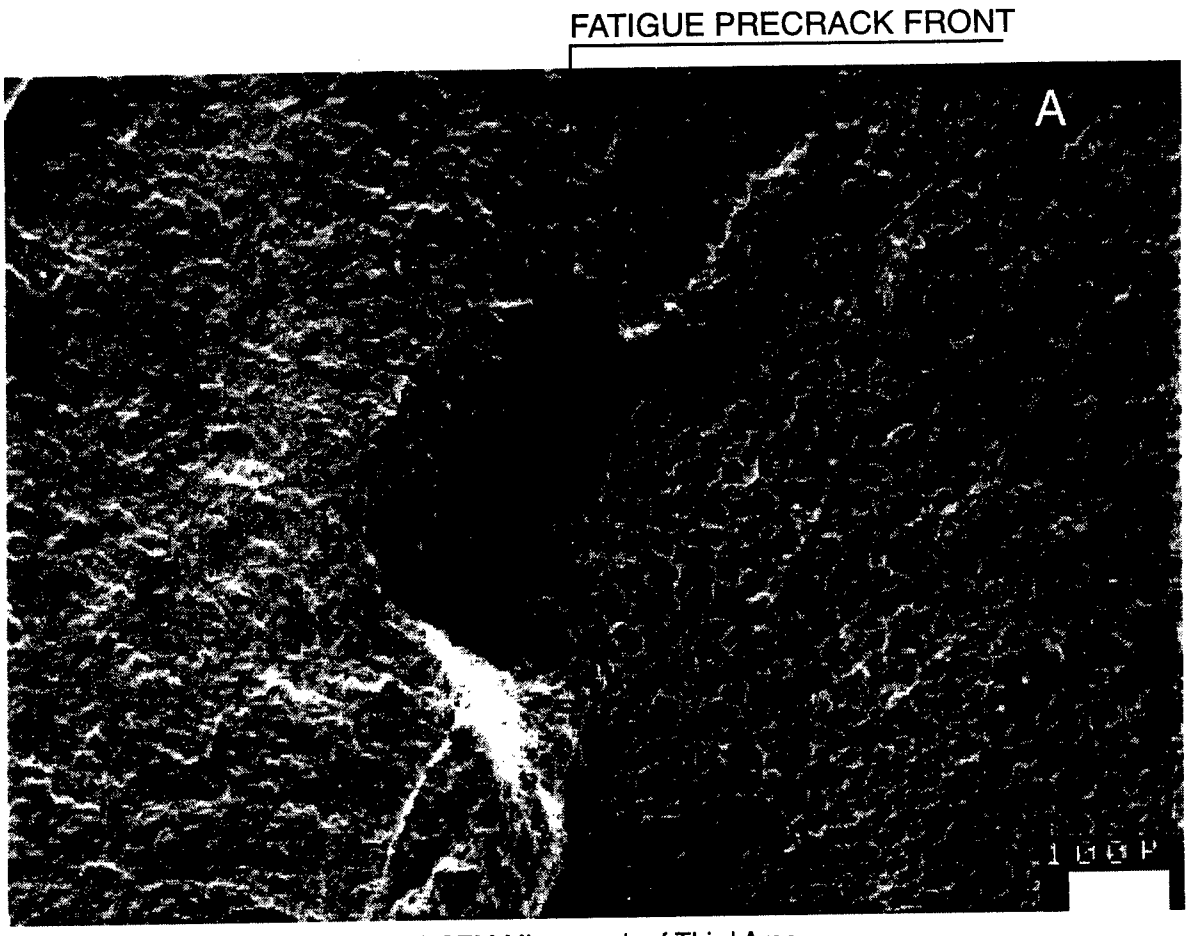

(a) SEM Micrograph of Third Area

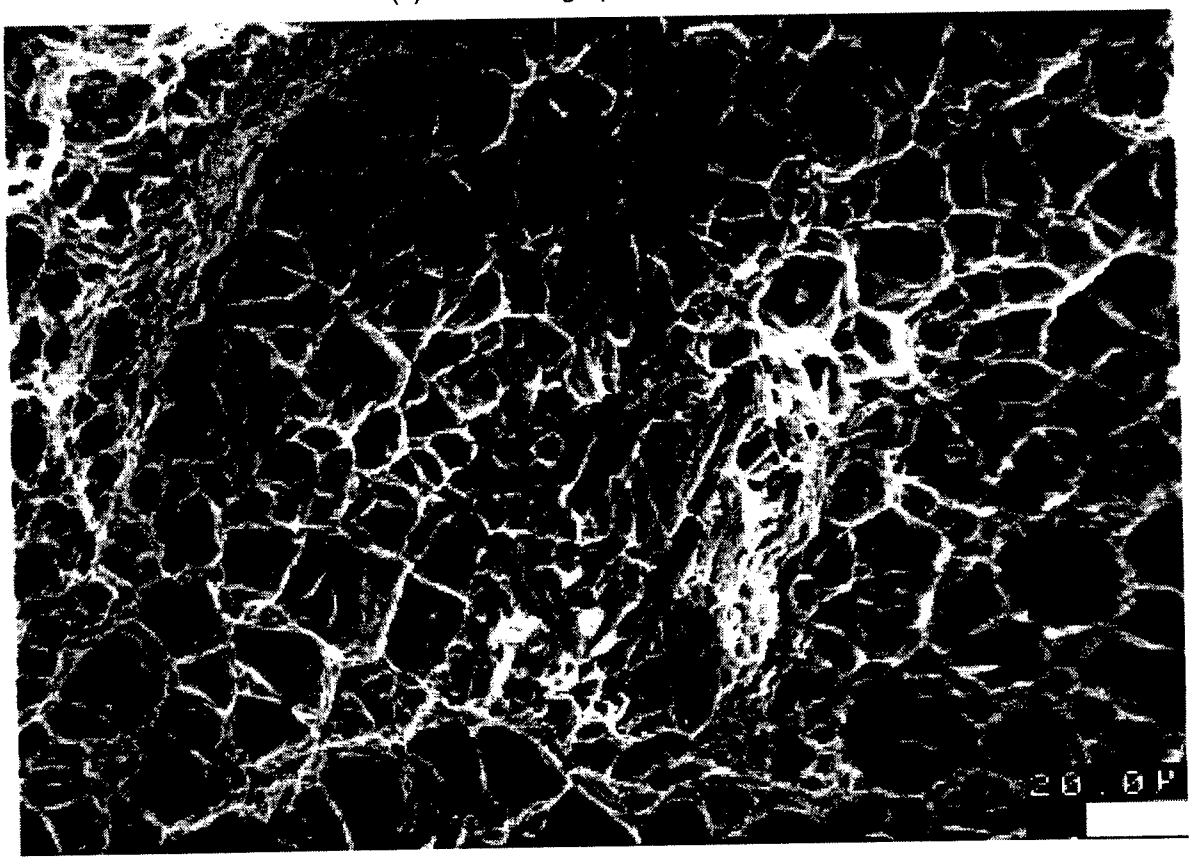

(b) Enlargement of Area A in (a)

Figure 21. SEM micrographs of the area where FRASTA detected third microcrack forming.

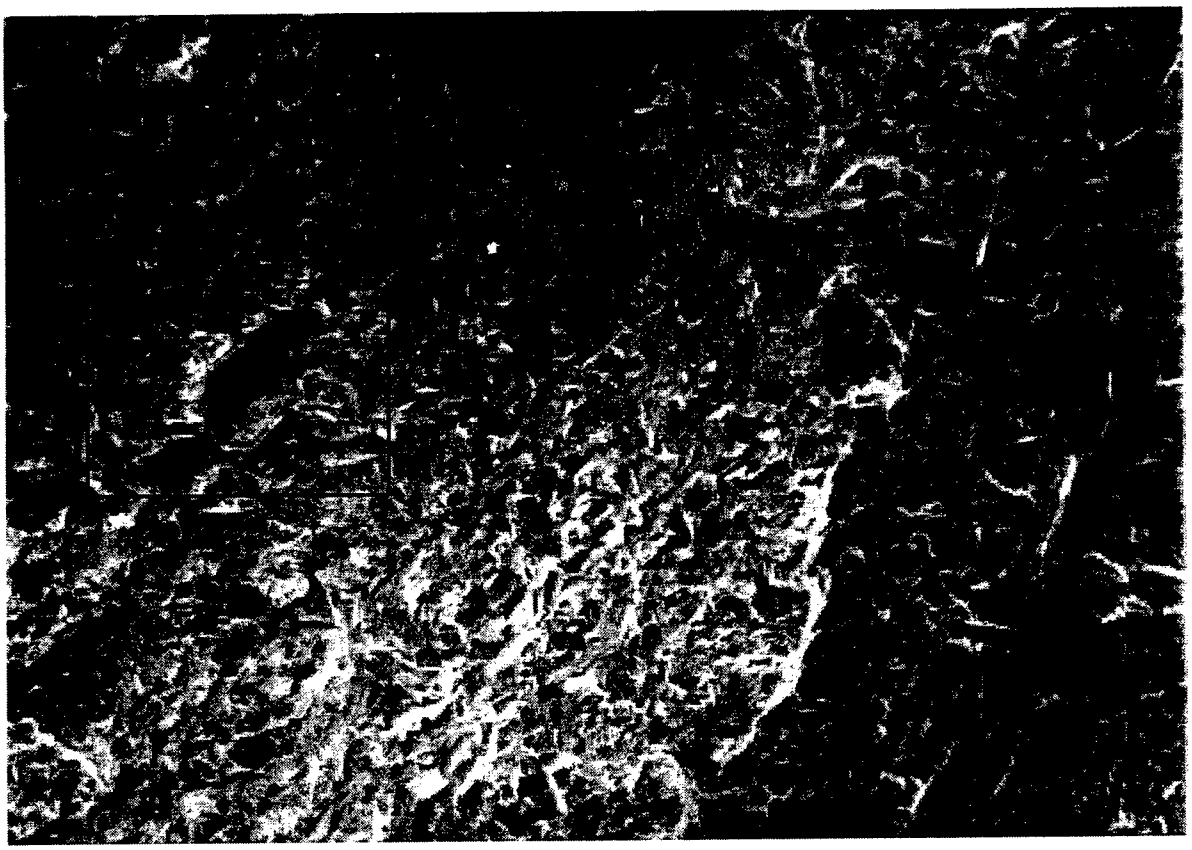

(a) SEM Micrograph of Site 4

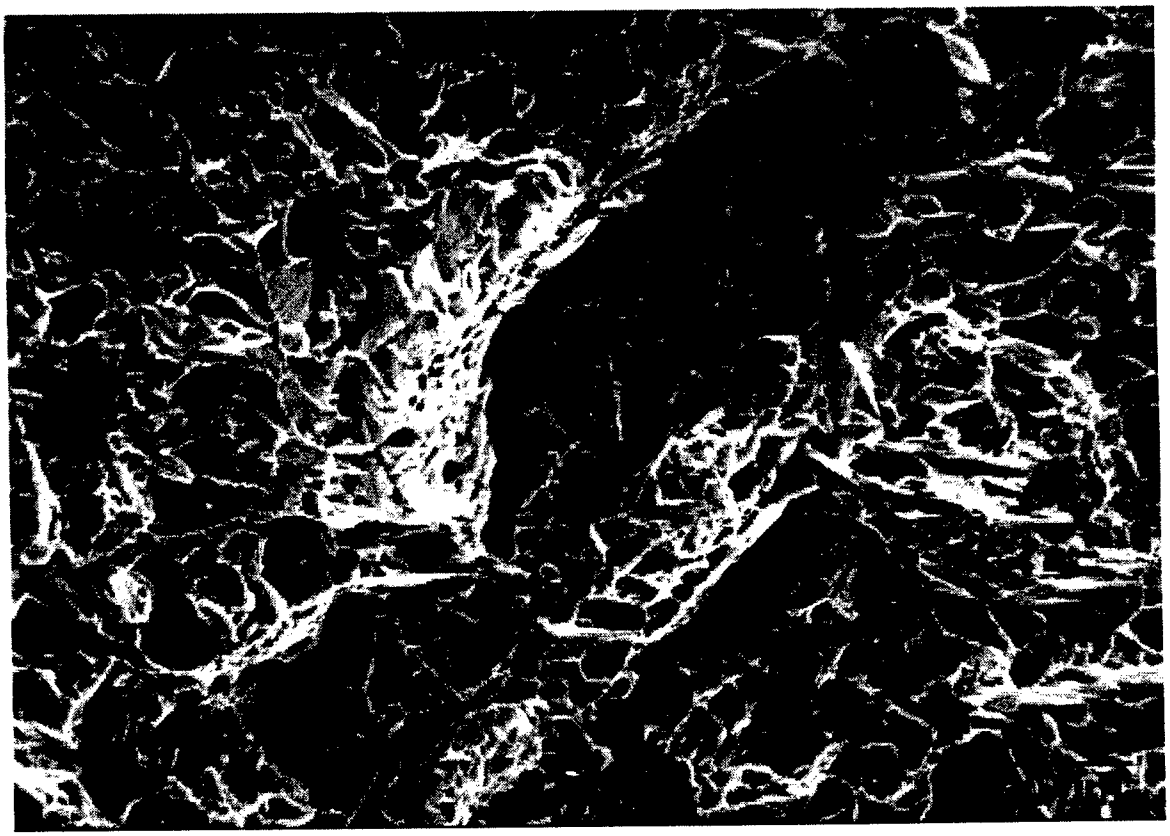

(b) Enlargement of Framed Area A in (a)

Figure 22. SEM micrographs of fourth area where FRASTA predicted microcracking activity.

DISCUSSION

Four microfailure initiation sites were identified by FRASTA and correlated with AE signals. Only one site (the fourth site, which occurred in the interior of the specimen) had an entirely brittle failure surface. The surfaces of each of the other three sites consisted of a field of uniformly sized ductile dimples, showing that failure was by the nucleation, growth, and coalescence of microvoids, a mechanism not considered to produce AE. However, within the sea of dimples for two of the sites (the first and the third) was a small, smooth-faceted area suggestive of brittle cleavage fracture. Because brittle fracture tends to suddenly release stored strain energy, these faceted sites are likely the sources of the recorded acoustic signals.

The second initiation site also contained a small cleavage surface among the dimples, but at a location somewhat removed from the point of microfailure nucleation. Therefore, we hesitate to consider this cleavage event as the source of the second AE signal. The FAPP's of figure 16 show that the development of the second initiation site was significantly faster than at Sites 1 and 3; however, the significance of ductile failure rate on AE is unclear.

In the process of confirming brittle microfailure sites in bridge weldments as origins of acoustic emission, a procedure was demonstrated for relating microfailure events to AE signals. The ability of FRASTA to relate microfailure activity to crack face spacing allows direct correlation of AE signals when AE is recorded as a function of specimen elongation and when elongation is concentrated in the plane of fracture.

This work also showed the significant role of local microstructure on the failure behavior of this bridge steel weldment. FRASTA indicated that microfailure initiated at three locations along the front of the fatigue precrack. At each location a large grain existed and was partially penetrated by the fatigue crack, and it was these grains that failed first. Two of these three grains were aligned with the dominant texturing direction of the macrostructure, and the field of fine dimples characterizing the surfaces of these failure sites was not observed elsewhere in the specimen.

The effort to correlate AE signals with microfailure origins is continuing. Bridge materials of simpler microstructure (nonwelded steels of compositions corresponding to A36, A572, and A7) will be examined using the test procedure described here, and advanced AE sensors and recording systems will be used that provide AE waveforms, instead of only acoustic amplitude and time of arrival data. Success in this effort will allow important and heretofore unobtainable information about fracture evolution to be extracted from AE spectra and will enhance the usefulness of AE monitoring of the Nation's bridges.

APPENDIX: THE FRASTA TECHNIQUE

Fracture surface topography analysis (FRASTA) is a computer-assisted technique for reconstructing the microdetails of a fracture event. The technique, which involves comparing the topographies of conjugate fracture surfaces, was created from a kinematic interpretation of microcrack evolution in a stressed material.

To understand how and why FRASTA works, consider the development of a microcrack in material during application of a load. Initially, the intact material undergoes local inelastic flow before failure begins in the form of a microvoid or microcrack at some weak spot or stress concentrator. The newly formed microfracture surfaces are free surfaces, so the tensile stresses on those surfaces fall to zero.* Thus, the material immediately beneath these surfaces undergoes no further plastic deformation in the local tensile direction. The applied load is redistributed to unfractured material in front of the crack tip, which continues to deform plastically until it, too, fractures.

Microfracture extension results from the continuing sequential process of deformation, microfracture, and redistribution of stresses. This sequential deformation and microfracture process produces differences in the amount of inelastic deformation existing at a given location in the material as a function of distance from the microfracture nucleation site. The variation in local inelastic deformation results in a surface irregularity (i.e., an elevation profile on the fracture surface) and provides a record of the history of the microfracture development. The fracture surface of a broken specimen or component contains many such irregularities, because macrofracture results from the nucleation, growth, and coalescence of many microfractures. Thus, the topography of the fracture surface provides a permanent record of the evolution of all the microfractures that contributed to the macrofracture surface.

The FRASTA technique accesses the information on microfracture evolution by first obtaining precise, quantitative, three-dimensional, topographic replicas of conjugate fracture surfaces from stereo photographs taken with an SEM or from direct profiling with a confocal scanning laser microscope (SLM). Then, a computer is used to compare the conjugate surface

* At this point, the released strain energy is dissipated in the material. If the microfailure event is sudden, as in brittle cleavage, the energy is released as a wave, which propagates through the material and may be detectable by an acoustic transducer at the material surface.

topographs to determine the amount of local inelastic deformation occurring before fracture. The information on the variation in the local inelastic deformation is used to reconstruct the microfracture activity from beginning to end.

Two ways of presenting FRASTA results are as a series of fractured-area-projection plots (FAPP's) and as a series of cross-sectional plots (XSP's). A FAPP (equivalent to an X-ray image taken perpendicular to the fracture plane) provides information on microcrack initiation sites and projected areas of micro/macrocracks. By examining a series of FAPP's, we can determine microcrack and macrocrack growth rates as a function of specimen deformation.

An XSP shows a section perpendicular to the fracture surface and displays the microcracks in profile. It shows how two surfaces match each other, the amount of overlap (inelastic deformation) necessary before fracture, and the amount of crack-face-opening displacement. Also obtained from the XSP is the cracktip-opening displacement, which can be correlated to the J-integral, or stress intensity factor, to determine the fracture toughness of the material. In some cases, it is possible to determine the loading conditions that caused the fracture.

The FRASTA technology has been applied to a wide range of failure problems in nearly all classes of materials. For a review of several applications, see references 5 and 6. Because the FRASTA technique can reconstruct the details of microfailure events occurring in the interior of a component and indicate their time sequence, it provides the heretofore lacking technology for correlating dynamic microfailure activity with the AE signals it produces.

REFERENCES

1. R. A. Livingston, C. Fortunko, M. Hamstad, T. Kobayashi, D. McColsky, and D. A. Shockey, "Digital Waveform-Based Acoustics Emission System for Nondestructive Testing of Steel Bridges," ASTM Conference, Boulder, CO, July 1996.

2. M. A. Hamstad and C. M. Fortunko, "Development of Practical Wideband High-Fidelity Acoustic Emission Sensors," Nondestructive Evaluation of Aging Bridges and Highways, S. Chase, Eds. (SPIE-The International Society for Optical Engineering, Bellingham, WA, 1995), pp. 281-288.

3. M. A. Hamstad, P. H. Thompson, and R. D. Young, "Acoustic Emission Source Location During Four-Point Bend Tests of Alumina," *Progress in Acoustic Emission III*, The Japan Society of NDI, pp. 26–33 (1986).

4. M. A. Hamstad, P. H. Thompson, and R. D. Young, "Flaw Growth in Alumina Studied by Acoustic Emission," *Journal of Acoustic Emission*, **6** [2] 93–97 (1987).

5. T. Kobayashi and D. A. Shockey, "FRASTA: A New Way to Analyze Fracture Surfaces, Part 1: Reconstructing Crack Histories," *Advanced Materials & Processes*, **140** [5] 28–34 (1991).

6. T. Kobayashi and D. A. Shockey, "Fracture Analysis via FRASTA, Part 2: Determining Fracture Mechanisms and Parameters," *Advanced Materials & Processes*, **140** [6] 24–32 (1991).

7. Y. Murakami, S. Aoki, N. Hasebe, Y. Itoh, H. Miyata, N. Miyazaki, H. Terada, K. Tohgo, M. Toya, and R. Yuuki, *Stress Intensity Factors Handbook, Volume 1*, pp. 42-43 (Pergamon Press, Japan, 1987)

8. Material Properties Standard 990, Coors Ceramic Company, Golden, CO, November 1990.

9. Nondestructive Testing Handbook, Volume Five: Acoustic Emission Testing, R. K. Miller and P. McIntire, Eds. (American Society for Nondestructive Testing, Columbus, OH, 1987), pp. 27-33.

10. National Technical Information Service, Proceedings of the Conference on Nondestructive Evaluation of Bridges, August 25, 1992, FHWA-RD-93-040A, Federal Highway Administration, McLean, VA, 1993.

11. M. G. Lozev, G. G. Clemena, J. C. Duke, and M. F. Sison, "Acoustic Emission Detection, Characterization and Monitoring of Steel Bridge Members," Structural Materials Technology: An NDT Conference, P. E. Hartbower and P. J. Stolarski, Eds. (Technomic Pub. Co., Lancaster, PA, 1996), pp. 323-328.

12. J. H. Giovanola, H. Homma, M. Lichtenberger, J. E. Crocker, and R. W. Klopp, "Fracture Toughness Measurements Using Small Cracked Round Bars," Constraint Effects in Fracture: Theory and Applications, ASTM STP 1244, M. Kirk and A. Bakker, Eds. (American Society for Testing and Materials, Philadelphia, 1994), pp. 255-285.

Reproduced by NTIS

National Technical Information Service
Springfield, VA 22161

This report was printed specifically for your order from nearly 3 million titles available in our collection.

For economy and efficiency, NTIS does not maintain stock of its vast collection of technical reports. Rather, most documents are printed for each order. Documents that are not in electronic format are reproduced from master archival copies and are the best possible reproductions available. If you have any questions concerning this document or any order you have placed with NTIS, please call our Customer Service Department at (703) 487-4660.

About NTIS

NTIS collects scientific, technical, engineering, and business related information — then organizes, maintains, and disseminates that information in a variety of formats — from microfiche to online services. The NTIS collection of nearly 3 million titles includes reports describing research conducted or sponsored by federal agencies and their contractors; statistical and business information; U.S. military publications; audiovisual products; computer software and electronic databases developed by federal agencies; training tools; and technical reports prepared by research organizations worldwide. Approximately 100,000 *new* titles are added and indexed into the NTIS collection annually.

For more information about NTIS products and services, call NTIS at (703) 487-4650 and request the free *NTIS Catalog of Products and Services*, PR-827LPG, or visit the NTIS Web site **http://www.ntis.gov**.

NTIS
Your indispensable resource for government-sponsored information—U.S. and worldwide

U.S. DEPARTMENT OF COMMERCE
Technology Administration
National Technical Information Service
Springfield, VA 22161 (703) 487-4650